J. Fluid Mech. (1990), *vol.* 217, *pp.* 41–69
Printed in Great Britain

Separation of a boundary jet in a rotating fluid

By MELVIN E. STERN[1] AND J. A. WHITEHEAD[2]

[1] Department of Oceanography, Florida State University, Tallahassee, FL 32306, USA

[2] Department of Physical Oceanography, Woods Hole Oceanographic Institution, Woods Hole, MA 02543, USA

(Received 8 November 1988 and in revised form 11 December 1989)

A semi-infinite jet flows along a vertical wall in a rotating fluid, with the nose of the intrusion approaching a corner where the wall turns through an obtuse angle $\theta+180°$. The jet separates at the corner and flows into the interior if θ exceeds a critical θ_c, otherwise part of the jet continues around the corner and flows along the downstream segment of the wall. The separation criterion is computed using an inviscid and piecewise-uniform-vorticity model, with s denoting the ratio of the maximum 'offshore' to 'inshore' vorticity. The separation effect is demonstrated by a laboratory experiment in which a two-dimensional jet flows along the wall from a source. Average velocities are used to estimate s, and to make semi-quantitative comparisons of experimental and theoretical θ_c. This suggests that the separation mechanism is independent of local viscous forces, although the cumulative effect of lateral eddy stresses in the jet is important in establishing the value of s immediately upstream from the corner. We suggest that our barotropic separation mechanism is relevant to mesoscale oceanic coastal currents.

1. Introduction

In a rapidly rotating homogeneous fluid it is possible to realize two-dimensional flows at large Reynolds number. A striking example of this occurs when a horizontal jet from a nozzle emerges at mid-depth in a tank of water rotating about a vertical axis (Flierl, Stern & Whitehead 1983). The three-dimensional turbulence of the emerging jet is suppressed downstream, where a depth-independent regime is established. A similar effect occurs when the nozzle is placed against a vertical wall, in which case a two-dimensional (but non-laminar) jet appears further downstream. The simple technique will be employed to demonstrate the unique kind of separation that can occur when a barotropic jet flows along a curved wall.

This is illustrated by the top view (figure 1, plate 1) of a 2 m diameter tank rotating counterclockwise, and containing 20 cm of water with a blue dye. The water emerging from the nozzles contains a black dye, and the jet becomes two-dimensional (see §6) well before the nose of the intrusion reaches the corner of the vertical wall, at which point the wall turns clockwise through an acute angle θ. Lateral instabilities and entrainment occur before the jet reaches the corner and the concomitant lateral eddy stresses determine the velocity profile in this region. When the nose reaches the corner (figure 1) it does not flow around it, but rather forms a dipolar vortex which propagates into the interior, and thereby establishes the path for the trailing jet.

This separation effect is not merely a simple consequence of the forward momentum of the jet, as is proven by the non-separating flow in figure 2 (plate 2), where all the conditions are the same as in figure 1 except that θ is reduced by half.

The white streaklines clearly show the flow of the jet around the corner. The black dye indicates both the progression of the wall jet further downstream, and also the large eddy which formed after the nose of the jet encountered the corner.

A horizontally non-divergent flow in an inviscid rotating fluid conserves relative vorticity (thereby giving rise to the paradox that the Coriolis parameter is parametrically unimportant for the temporal evolution of a given initial state, even though the rapid rotation is crucial for vorticity conservation). We shall use this two-dimensional theory to obtain an explanation of the separation process (figure 1), and a semi-quantitative prediction of a critical $\theta = \theta_c$. In addition, we shall employ a piecewise-uniform vorticity model of a semi-infinite wall jet, with s denoting the magnitude of the 'offshore'/'inshore' vorticity ratio. These positive and negative vorticity layers are separated by an interface (subsequently designated $l = 1$), and another interface ($l = 2$) separates the outer layer of the jet from an irrotational region of semi-infinite extent. The two interfaces intersect the wall at a common nosepoint, which advances into the irrotational fluid and thereby displaces this fluid up, over, and behind the nose (cf. the streaklines in figures 1, 2).

The evolution of $l = 1, 2$ will be computed by a conformal mapping of the contour dynamical equations, starting from an assumed initial state which is chosen to isolate the (local) separation process and to avoid the problem of the evolution of the jet from its source. This larger problem requires a consideration of the two-dimensional instability of a wall jet, and the subsequent entrainment of irrotational fluid. To some extent these effects are parameterized in our theory by the value of s assumed for the inviscid jet. Although the fluid in our theory is free to slip at the wall, it is obviously desirable to assume vanishing wall velocity far upstream in the undisturbed region of our semi-infinite jet, since this assumption incorporates an important feature of a real boundary jet. In order to focus on the separation mechanism we shall restrict the initial position of the nosepoint to lie at a rather small distance upstream from the corner. Although our emphasis is on the physical mechanism rather than a definitive quantitative separation criterion, evidence will be presented showing that the assumed structure of the initial state is not of overriding importance.

The mechanism by which our jet separates is different from the two-dimensional (and low Reynolds number) flow of a free stream around a curved wall (Smith 1986; Dennis & Chang 1970), where the adverse pressure gradient produced by the free stream, acting in conjunction with the local viscous force in the boundary layer, generates vorticity of the opposite sign from that existing upstream. In our problem there is no free stream (and no viscosity), but vorticity of both signs exists in the jet upstream from the separation point. In this case flow separation is produced by the inviscid effect of wall curvature on the vortex elements in the two-dimensional jet.

The basic fluid dynamical problem treated herein may be useful in studying oceanic coastal flows, where high-Reynolds-number and quasi-two-dimensional flows prevail, even though other physical factors like buoyancy enter. For example, Shen's (1981) laboratory experiments show that when density effects are important the interface between two fluids can be displaced vertically until it intersects a horizontal boundary, whereupon the flow can separate from the vertical wall. A similar effect may occur in the Gulf Stream (Parsons 1969; Ou & de Ritter 1986). Our purely barotropic process may be more directly relevant to somewhat smaller scales, such as occurs in the vicinity of capes and straits (Roed 1980).

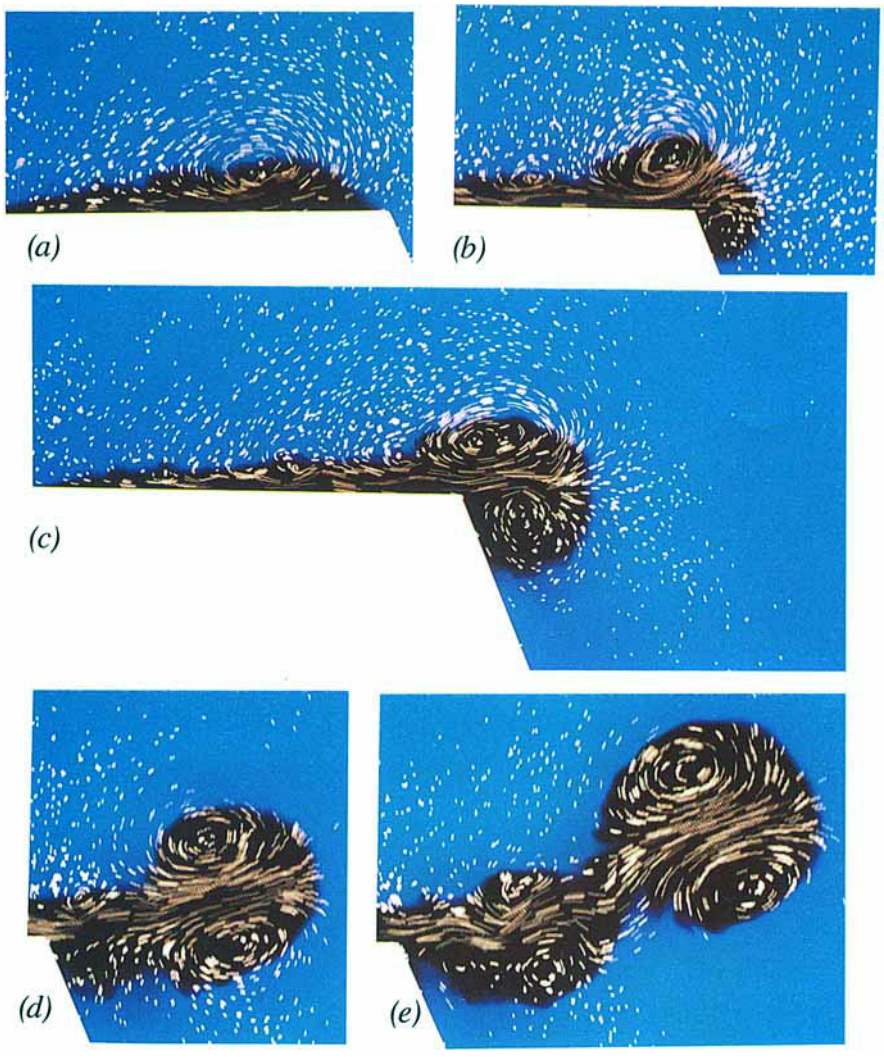

FIGURE 1. Top view of a jet (black) flowing from small nozzles mounted flush against a vertical wall and into ambient water (blue) in a tank rotating with period T=15.1 s. The water depth is 20 cm, the nozzle flow rate is Q=14.3 cm^3/s and the nozzles are located 70 cm upstream from the corner of the wall, whose downstream segment turns through a clockwise angle θ=60°. A 1 s time exposure has been used to obtain the streaks of the small white paper pellets on the free surface. (*a*) t=16 s after the nozzle flow starts. Note the streaks in the blue water which reveal the irrotational velocity in the ambient fluid as it is pushed up and over the nose of the jet. Counterclockwise vorticity exists in the outer part of the black dye, clockwise vorticity exists in the inner part, and the downcoast velocity u is non-negative everywhere near the wall. (*b*) t=22 s. As the nose encounters the corner small negative u appears downstream from the corner. (*c*) t=28 s. A small region of clockwise circulation, detached from the wall, forms downstream of the corner. (*d*) t=40 s. This clockwise circulation on the inside of the jet increases in strength and combines with the large counterclockwise circulating region on the outside to form a dipole. Behind this dipole, relatively large u occurs in the current at the corner. (*e*) t=55 s. The dipole continues propagating into the interior and the jet at the corner continues to separate. The small amount of black dye downstream from the corner retreats, and no particles from the jet flow along the downstream wall at later times. Two-dimensional eddies are generated by the separated jet, which also forms a large and relatively weak recirculation gyre. This supplies the water entrained by the jet before it reaches the corner.

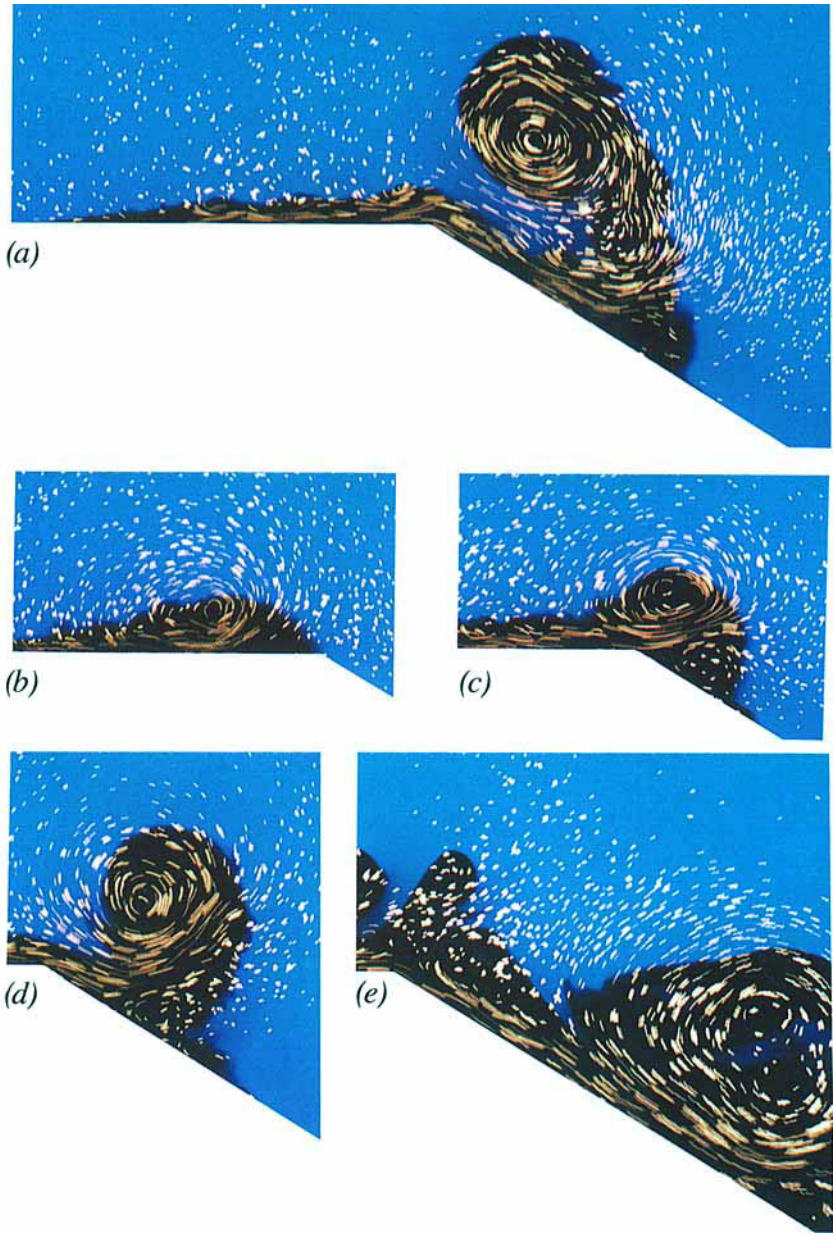

FIGURE 2. Same as figure 1 except $\theta=30°$. This smaller θ produces a non-separating flow which continues along the downstream segment of the wall. Please note that the first frame listed below is presented out of its normal time sequence for purposes of emphasis and clarity. (*a*) $t=48$ s. This frame most clearly reveals the difference between the separating and non-separating regimes. At this time a strong wall current ($u>0$) exists at and downstream from the corner. This is accompanied by a large counterclockwise offshore eddy, but there is no clockwise circulation region corresponding to that in figure 1. (*b*) $t=15$ s. This photograph, and the two following ones show the shape of the jet prior to (*a*). (*b*) is indistinguishable from figure 1(*a*). (*c*) $t=24$ s. This state is also not different from figure 1(*b*). (*d*) $t=36$ s. This is the state before (*a*) (above) and it shows the black dye of the coastal current proceeding past the corner. (*e*) $t=84$ s. Notice that the large counterclockwise eddy has moved parallel to the coast, and strong downstream currents still occur at the corner, along with patches of dye left behind by the large eddy.

2. Elementary considerations

Since a jet consists of many vortices of opposite sign, it is instructive to consider first the conditions under which a dipole, composed of equal and opposite point vortices displaced from each other by a distance $\sigma(t)$, will separate from the wall by moving to infinity as time (t) increases. In the simplest case (Acton 1976) the wall is completely straight, and its upward normal is rotated through a clockwise angle $e(t)$ from the upward normal to the dipole axis. Suppose the counterclockwise circulating member of the dipole is closer to the wall than the clockwise member. Then for any $e(0) > 0$ there exists a sufficiently small $\sigma(0)$ such that the dipole will eventually move to an infinite distance from the wall (i.e. 'separate'), because the mutual interaction of the vortices in the dipole exceeds the effect of their images.

For the case of irregular boundaries (see Sheffield's 1957 calculation of the separation of a monopolar point vortex emerging from the end of a channel) we consider figure 3, which generalizes Acton's problem by having a corner in the wall at $\zeta = 0$ (in the complex plane), and with $\{z_+(t),\ z_-(t)\}$ denoting the complex coordinates of the two vorticies. An appropriate and instructive initial condition in the context of our continuum problem (see §3) is: $z_+(0) = i$, $z_-(0) = i + i\sigma(0)$. For any $\alpha > 1$, and for $\sigma(0)$ sufficiently small, it is once again clear that the mutual interaction of the vortices will dominate over wall-induced motion, and the dipole will move coherently to $|\zeta| = \infty$. The critical $(\alpha, \sigma(0))$ for this separation was computed using a conformal mapping, and the results are indicated in the Appendix.

The next instructive problem is provided by the stream function produced by a point vortex outside a circular wall. We know from potential theory that this boundary may be replaced by the vortex image located at the 'inverse' point, which is located nearer to the circumference than the vortex. Therefore the maximum tangential speed at the circular wall increases as the wall curvature increases, provided the distance of the vortex from the wall remains constant.

Let us apply this result to the qualitative determination of the motion of the nosepoint of a jet (figure 4*a*) flowing around a smoothly curving wall. The clockwise (negative) vortex in each area element of the outer part of the jet induces a downstream velocity at the nosepoint, whereas each anticlockwise (positive) element in the inner part (wall side) tends to move the nosepoint upstream. Although both tendencies increase with wall curvature, the latter one will dominate if the positive layer is sufficiently thick and if the negative vortices are relatively far from the nose. On the other hand, if the positive layer is entirely removed ($s = 0$) then the resulting half-jet with negative vorticity cannot separate from the wall, and the nosepoint must continue moving down the coast no matter how large its curvature. Thus we see that a sufficiently large s will cause the fluid near the nosepoint to stagnate (or even move upstream), while the fluid near the axis of the jet tends to continue downstream (figure 4*b*). Consequently the oncoming positive vorticity in the jet leaves the coast, flows offshore, and forms a 'positive' eddy near the leading edge of the jet. As the area and total vorticity of this eddy increase, it deflects the overlying negative-vorticity fluid from its downstream path, causing some of this fluid to reverse direction by flowing upstream and to be entrained into the positive eddy. The next phase (figure 4*c*) depends on the wall curvature being sufficiently large, and its enhancement of the positive eddy sufficiently great, so that the ambient irrotational fluid is also entrained. If this occurs then no particle on either side of the jet axis makes contact with the wall downstream from the separation point. Consequently the negative vorticity in the upstream fluid must also pile-up, thereby forming a

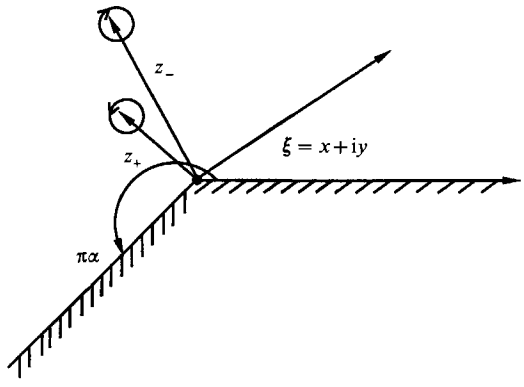

FIGURE 3. A cyclonic point vortex is located at $z_+(t)$ in the complex plane, and an anticyclonic point vortex is located at $z_-(t)$. Initially $z_+(0) = i$, $z_-(0) = [1+\sigma(0)]\,i$, and the question is what values of $\alpha, \sigma(0)$ lead to the dipole separating from the curved wall.

negative eddy over the positive one. At this stage of our qualitative argument the leading edge of the jet consists of a dipole at such a large distance from the wall that the mutual interaction will propel the dipole further away from the wall (as suggested by figure 3 and by the Appendix).

This qualitative picture will be supported (§3) by inviscid calculations for a piecewise-uniform-vorticity jet flowing towards a 'sharp' coast (cf. figure 5*a*), which has all the curvature concentrated at one point. The velocity is singular here, but integrable, and the streamline pattern produced by a vortex element is qualitatively similar to what would be produced at a smoother wall. Thus the sharp coast model in §3 is the simplest one, and this is also the case for the experiment (§6) since it involves fewer independent non-dimensional parameters than a smoothly curving coast.

Our calculations utilize the well-known contour-dynamics method to compute the evolution of two interfaces bounding three piecewise-uniform-vorticity domains, two in the jet and one in the ambient irrotational fluid. A novel feature arises because of the spatial inhomogeneity of the Green's function for the velocity produced by an elementary vortex in the presence of an irregular boundary, since this prevents us from reducing the two-dimensional evolutionary problem to a one-dimensional problem (for the contours). Instead, the Green's function must be numerically integrated across the stream as well as along the stream, in order to obtain the instantaneous velocity of Lagrangian points on each interface. Nevertheless the contour-dynamical method is still relatively efficient and useful for several reasons, not the least of which is the ability to focus on the purely inertial character of the separation in the absence of viscosity. (NB, Please excuse the different orientation of the jet in figure 1 and in the following theory, where it makes no difference which way the jet flows).

3. Contour dynamics for a jet on a bent coast

The outer interface (denoted by $l = 2$ in figure 5) separates the ambient irrotational fluid from the negative-vorticity layer of the jet, which has unit non-dimensional thickness at $x_p = \infty$, and a non-dimensional vorticity equal to -1. Below the lower interface ($l = 1$) of this layer there is a positive layer having vorticity $1/s$ and

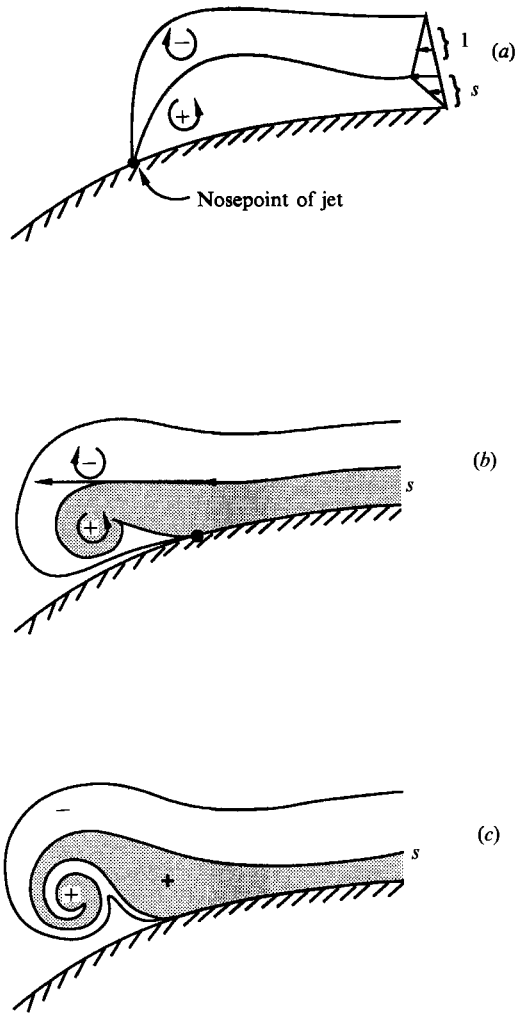

FIGURE 4. Schematic diagram of the separation process for a jet intruding into an irrotational fluid along a curved wall (see text).

thickness s at $x_p = \infty$. In general the fluid may slip at the walls, but for previously mentioned reasons we choose the undisturbed jet profile such that $u_p(\infty, 0) = 0$, as in figure 5. Far upstream the maximum jet velocity equals unity, and the scale for non-dimensional time t is the reciprocal of the vorticity below $l = 2$. For $t > 0$ the common nosepoint at $y_p = 0$ will move leftwards in the complex 'physical' space (figure 5*a*) approaching the corner $z_p = x_p + iy_p = 0$, $(2\pi > \arg z_p \geqslant 0)$.

The complex velocity $u_p + iv_p$ is obtained by summing the contributions of the vorticity elements in the area $d\xi_p\, d\eta_p$, located at $\zeta_p = \xi_p + i\eta_p$. This element produces a velocity field with vanishing normal velocity on the wall and vanishing velocity at $y_p = \infty$. It is convenient to express the total vorticity field as the sum of two overlapping layers, each of which is bounded below by the wall. The first layer is upper-bounded by interface $l = 2$, and is assigned vorticity -1; the second layer is upper-bounded by $l = 1$, and is assigned vorticity $(1 + 1/s)$, so that the join of the two layers yields a net vorticity $1/s$ below $l = 1$.

Let the stream function be such that its x_p derivative equals $+v_p$. If an overbar is used to denote a complex-conjugate then the typical area element of the first field will produce a contribution to the total stream function given by the imaginary part of

$$(-1)\,\mathrm{d}\xi_p\,\mathrm{d}\eta_p\left(\frac{\mathrm{i}}{2\pi}\right)[\ln(z_p^\beta-\zeta_p^\beta)-\ln(z_p^\beta-\overline{\zeta_p^\beta})],\quad \beta=\frac{1}{\alpha}, \tag{3.1a}$$

because z_p^β is (negative) real on the downstream half ($x_p<0$) of the wall, and thus the imaginary part of (3.1a) vanishes everywhere on the wall. Furthermore (3.1a) vanishes at $y_p\to\infty$, and as $z_p\to\zeta_p$ we obtain the limit

$$\ln(z_p^\beta-\zeta_p^\beta)\to\ln(\beta\zeta_p^{\beta-1}(z_p-\zeta_p))\to\ln(z_p-\zeta_p),$$

which implies that the imaginary part of (3.1a) is the stream function produced by a vorticity equal to (-1) inside $\mathrm{d}\xi_p\,\mathrm{d}\eta_p$. Likewise

$$\left(1+\frac{1}{s}\right)\mathrm{d}\xi_p\,\mathrm{d}\eta_p\left(\frac{\mathrm{i}}{2\pi}\right)[\ln(z_p^\beta-\zeta_p^\beta)-\ln(z_p^\beta-\overline{\zeta_p^\beta})] \tag{3.1b}$$

is the stream function produced by a typical area element of the second field. The sum of the integrals of (3.1a,b) gives the complex velocity potential at z_p, and the derivatives of this function of z_p gives the negative conjugate of the complex velocity, i.e.

$$-\overline{(u_p+\mathrm{i}v_p)}=\frac{\mathrm{i}\beta(1+1/s)}{2\pi}\iint_{l=1}\mathrm{d}\xi_p\,\mathrm{d}\eta_p\,z_p^{\beta-1}\left(\frac{1}{z_p^\beta-\zeta_p^\beta}-\frac{1}{z_p^\beta-\overline{\zeta_p^\beta}}\right)$$
$$-\frac{\mathrm{i}\beta}{2\pi}\iint_{l=2}\mathrm{d}\xi_p\,\mathrm{d}\eta_p^\beta\,z_p^{\beta-1}\left(\frac{1}{z_p^\beta-\zeta_p^\beta}-\frac{1}{z_p^\beta-\overline{\zeta_p^\beta}}\right), \tag{3.2a}$$

where $l=2$ indicates that the integration extends over the entire area bounded by that interface. From now on z_p will denote a Lagrangian point on an interface, so that

$$u_p+\mathrm{i}v_p=\frac{\mathrm{d}z_p}{\mathrm{d}t} \tag{3.2b}$$

and thus we obtain two integro-differential equations for Lagrangian points on $l=1$ and $l=2$.

It is more convenient to perform the integrations (3.2a) in the conformally mapped space of figure 5(b), wherein the wall is straight (but the mapped interface far upstream are no longer straight). The mapped space coordinates have no subscript and are denoted by

$$\zeta=\xi+\mathrm{i}\eta=\zeta_p^\beta,\quad z=x+\mathrm{i}y=z_p^\beta.$$

and the inverse relations are

$$\zeta_p=\zeta^\alpha,\quad z_p=z^\alpha.$$

By introducing the Jacobean transformation

$$\mathrm{d}\xi_p\,\mathrm{d}\eta_p=\mathrm{d}\xi\,\mathrm{d}\eta\begin{vmatrix}\partial(\mathrm{Re}(\zeta^\alpha))/\partial\xi & \partial(\mathrm{Im}(\zeta^\alpha))/\partial\xi\\ \partial(\mathrm{Re}(\zeta^\alpha))/\partial\eta & \partial(\mathrm{Im}(\zeta^\alpha))/\partial\eta\end{vmatrix}=\alpha^2|\zeta^{\alpha-1}|^2\,\mathrm{d}\xi\,\mathrm{d}\eta, \tag{3.3}$$

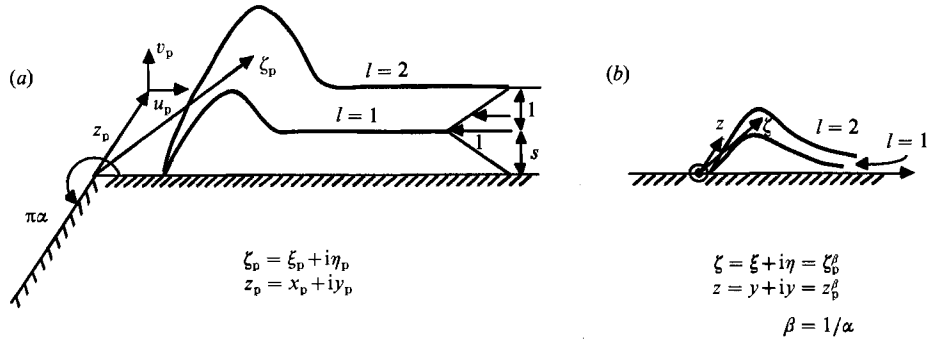

FIGURE 5. Definitional diagram of a piecewise-uniform-vorticity jet flowing towards the corner ($\zeta_p = 0$) of the wall. (*a*) Physical space with (u_p, v_p) denoting the velocity components at $z_p = x_p + iy_p$. (*b*) The conformal mapping straightens the boundary and distorts the interfaces.

and by using
$$\frac{dz_p}{dt} = \alpha z^{\alpha-1}\frac{dz}{dt}$$

in (3.2) we get

$$\frac{2\pi\, dz}{dt} = \frac{i}{|z|^c}\left[\left(1+\frac{1}{s}\right)\iint_{l=1} d\xi\, d\eta\, |\zeta|^c\left(\frac{1}{\bar{z}-\bar{\zeta}}-\frac{1}{\bar{z}-\zeta}\right) - \iint_{l=2} d\xi\, d\eta\, |\zeta|^c\left(\frac{1}{\bar{z}-\bar{\zeta}}-\frac{1}{\bar{z}-\zeta}\right)\right], \tag{3.4}$$

where
$$c = 2(\alpha-1).$$

This is to be computed for all Lagrangian points $z = z(I, k)$ on the lower ($k = 1$) interface and on the upper ($k = 2$) interface, thereby obtaining $2Ik$ ordinary equations for the (approximate) temporal evolution of these interfaces in mapped space.

We note that as the nosepoint passes the corner ($z = 0$), (3.4) has an integrable singularity. For any other position of the nosepoint ($\mathrm{Im}\,(z) = 0$) both integrands in (3.3) are pure negative imaginary numbers ($\mathrm{Im}\,(\zeta) > 0$), so that the contribution of the $l = 1$ integral to the nose velocity is positive, and the contribution of the $l = 2$ integral is negative. Thus the negative vortices in the jet tend to move the nose downstream (past the corner), whereas the positive vortices tend to move the nosepoint upstream thereby blocking the oncoming flow. If the former effect dominates, such as will occur when $s = 0$, then no 'separation' will occur. But when s and α are sufficiently large the positive vortices should control the nose velocity near the corner point, and separation should occur.

For a point on $k = 1$ in (3.4) the $l = 2$ integration encounters an interior singularity which poses a numerical problem. This was resolved by introducing the identities;

$$\frac{|\zeta|^c}{z-\zeta} = \frac{|z|^c}{z-\zeta} - \frac{(|z|^c - |\zeta|^c)}{z-\zeta};$$
$$\frac{|\zeta|^c}{z-\bar{\zeta}} = \frac{|z|^c}{z-\bar{\zeta}} - \frac{(|z|^c - |\zeta|^c)}{z-\bar{\zeta}}.$$

When $\zeta \to z \neq 0$ the last term in the first of these equations approaches the *finite* limit:

$$\lim_{z\to\zeta}\frac{|z|^c - |\zeta|^c}{z-\zeta} = -ic\,|z|^{c-2}\,\mathrm{Im}\,(z) \quad (c < 2, |z| > 0)$$

and only a simple pole appears in the remaining term of the first identity. When these identities are used in (3.4), we may write the result as

$$\frac{\mathrm{d}z(I,k)}{\mathrm{d}t} = \frac{1}{2\pi}[A(I,k)+B(I,k)]+\frac{1}{2\pi}[P(I,k)-T(I,k)], \tag{3.5}$$

where
$$A(I,k) = \frac{-\mathrm{i}(1+1/s)}{|z(I,k)|^c}\mathrm{CONJG}\iint_{l=1} \mathrm{d}\xi\,\mathrm{d}\eta\left[\frac{|z|^c-|\zeta|^c}{z-\zeta}-\frac{|z|^c-|\zeta|^c}{z-\bar{\zeta}}\right], \tag{3.6a}$$

$$B(I,k) = \frac{\mathrm{i}}{|z|^c}\mathrm{CONJG}\iint_{l=2} \mathrm{d}\xi\,\mathrm{d}\eta\left[\frac{|z|^c-|\zeta|^c}{z-\zeta}-\frac{|z|^c-|\zeta|^c}{z-\bar{\zeta}}\right] \tag{3.6b}$$

have non-singular integrands, and where

$$P(I,k) = \mathrm{i}\left(1+\frac{1}{s}\right)\mathrm{CONJG}\iint_{l=1} \mathrm{d}\zeta\,\mathrm{d}\eta\left(\frac{1}{z(I,k)-\zeta}-\frac{1}{z-\bar{\zeta}}\right), \tag{3.7a}$$

$$T(I,k) = \mathrm{i}\,\mathrm{CONJG}\iint_{l=2} \mathrm{d}\xi\,\mathrm{d}\eta\left(\frac{1}{z-\zeta}-\frac{1}{z-\bar{\zeta}}\right) \tag{3.7b}$$

can be integrated in η, thereby reducing them to single contour integrals. When $\alpha = 1, c = 0, A(I,k) = B(I,k) = 0$, and (3.7) with (3.5) give the velocity for a jet flow along a straight coast (Stern 1989). Thus we may appropriate the algorithm tested and used in that paper for evaluating $P-T$ when $c \neq 0$. The only modification is due to the subsequent truncation of the integrals at finite x, which requires a correction for the effect of the far field ($x \to \infty$). These and other details of the numerical calculation are discussed below, but the reader may prefer to skip to §4.

The computation of (3.6*a*, *b*) requires an η-integration at each ξ, which was done by dividing the ordinate under each interfacial point into a number of segments (increasing with the value of the ordinate) of equal height, and then using a trapezoidal approximation. Another trapezoidal approximation was then used for the ξ-integration, which was generally truncated at $x_\mathrm{p} = 10.2$. The region beyond this is called the far field or the 'wings', the region $8.2 < x_\mathrm{p} < 10.2$ is called the 'intermediate' field, and $x_\mathrm{p} < 8.2$ is the 'near' field.

To the truncated near-field value of $A(I,k)+B(I,k)$ must be added the contribution $W(I,k)$ of the far field, which was computed by assuming undisturbed far-field interfaces. Then in the W integrands we set $\zeta(\xi)$ equal to the mapping of $y_\mathrm{p} = s$ or $y_\mathrm{p} = 1+s$, and the resulting integrals yields the asymptotic (for $|z_\mathrm{p}|/\xi_\mathrm{p} \ll 1$) result:

$$W(I,k) = \beta^2 s^2\left(1+\frac{1}{s}\right)G_1^{-1}|z(I,k)|^{-c}\left(1-\left|\frac{z}{G_1}\right|^c\right)-\beta^2(1+s)^2G_2^{-1}|z|^{-c}\left(1-\left|\frac{z}{G_2}\right|^c\right),$$

$$G_l = \mathrm{Re}\,[z[NN(l),l]],$$

where $NN(l)$ denotes the integral index of the last Lagrangian point ($\mathrm{G}_l \sim x_\mathrm{p}^\beta$) on $l = 1, 2$. (This expression is asymptotically valid when $G_l \to \infty$ with $z = z(I,k)$ fixed, and the only reason for retaining the term $|z/G_l|^c$ was to ensure that $W(I,k) = 0$ when $c = 0$). A similar procedure was used to augment the truncated value of $P(I,k)-T(I,k)$ with the far-field contribution.

These asymptotic wing corrections are not valid in the intermediate field, and consequently points in the latter region were merely moved in mapped space in such a way that their velocity in physical space was equal to that which was computed for the last near-field point (i.e. the one at $x_\mathrm{p} \approx 8.2$). The validity of this joining

procedure was checked by examining the smoothness of the computed interfaces (this is a good test because of the inherent instability of a jet to small perturbations). Furthermore, the main region of interest is in the vicinity of $z = 0$, and in the limited time interval when separation occurs.

Now we turn to the question of choosing the initial conditions in such a way that our highly idealized model will be able to capture the more complex separation effect which occurs in the realization (§6). First, the initial position of our nosepoint should be reasonably near $x_p = 1$, for otherwise (if $x_p \gg 1$) we should be focusing on the different problem (cf. figure 6) of flow over a straight coast, in which other eddy effects occur. Secondly, the leading edge of the intrusion should have significant and comparable amounts of total positive and negative vorticity in the nose region of the intruding jet. This corresponds to the structure of the real jet as it approaches the corner, and we previously agreed that it was reasonable to assume this structure in the initial conditions of our problem.

When the common nosepoint of the interfaces approaches $\zeta = 0$, the corresponding values of A, B become very large (although the velocity singularity is integrable in time). The numerical problem that this poses was resolved by a simple smoothing procedure, such that when $|z(I,k)|$ was less than some preassigned small value (e.g. 0.025). The value of $|z(I,k)|^c$ in the denominator of $(3.6a,b)$ was reset to $\mathrm{Im}\,[z(I,k)] = 0.025$ (keeping $\mathrm{Re}\,[Z(I,k)]$ unaltered). This has the effect of reducing the magnitude of the horizontal velocity of the nosepoint (only) when it is near the corner, but it does not alter the velocity at any overlying Lagrangian point (if $\mathrm{Im}\,(z) > 0.025$).

The temporal change of the z-points was computed using a second-order Runge–Kutta integration with a time step $T = 0.1$ (except in one comparison case where $T = 0.05$). After each T, Lagrangian points were inserted or deleted, depending on whether neighbour separation was too large or too small. The spacing of points was designed to maintain a nominal 1% accuracy in the computed velocity (see Stern 1989 where analytical comparison are given).

4. Numerical results for limiting cases

First we consider a jet intruding along a straight coast ($\alpha = 1$), in which case we set $c = 0 = A(I,k) = B(I,k)$. A single short computation for this case has been given by Stern (1989) (in the context of the problem of vorticity frontogenesis) using the initial 'sharp nose' interfacial ordinates:

$$y_p(x,0) = \begin{cases} s(1-\exp[-2(x_p-1)]), & x \geqslant 1, \quad l = 1, \\ (1+s)\,(1-\exp[-2(x_p-b)]), & x \geqslant b, \quad l = 2, \end{cases} \tag{4.1}$$

and with $b \neq 1$ (non-coincident nosepoints). A comparison of results was made to check the numerical program for (3.5), and then we made the small modification for the common ($b = 1$) nosepoint condition used here. Some discussion of the results for this case is necessary for understanding the $\alpha \neq 1$ problem.

Figure 6 shows that for $s = 0.50$ the maximum ordinate of $l = 2$ is much larger than its value at $t = 0$ (*equation* (4.1)). This is due to the dominant influence of the (nearby) negative vortices on particles at the nose of $l = 2$, so that a net upward motion is produced there. As negative vorticity accumulates under $l = 2$, downward velocities are induced in the rear of the bulbous nose. This results in a trough on $l = 2$, which eventually evolves into a thin filament (figure 6) carrying irrotational fluid into the nose. There is also a very thin (and dynamically negligible) filament

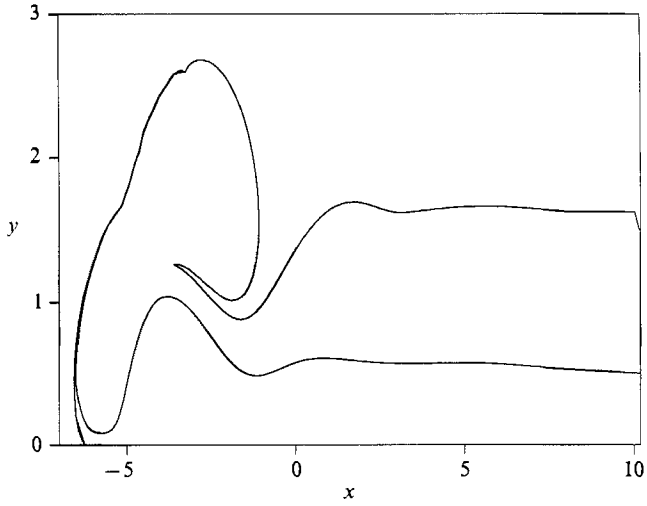

FIGURE 6. The contour dynamical calculation at $t = 20$ for a straight boundary ($\alpha = 1$) for $s = 0.50$, and for the 'sharp nose' initial condition (4.1). At $t = 0$ the nosepoint was at $x = 1$ (note vertical exaggeration). A large negative eddy is in the process of forming between the upper interface ($l = 2$) and the lower one ($l = 1$). In this and all subsequent figures the subscript p on x and y has been discarded. Also note the thin filament from $l = 1$ which has been 'captured' and passively advected along the leading edge of $l = 2$.

from $l = 1$ which is almost coincident with the $l = 2$ nose, but the main part of the leading edge of $l = 1$ has been displaced away from $l = 1$. This important effect is due to the dominant influence of the positive vortices lying underneath $l = 1$. The downstream motion of the leading edge of the entire intrusion is therefore mainly determined by the negative vorticity in the $l = 2$ nose.

Since the sharp-nose initial condition is not very realistic, and since it produces the computationally undesirable feature of the very thin $l = 1$ filament, we proceeded to use the 'blunt nose' profile:

$$y_{\mathrm{p}}(x,0) = \begin{cases} s(1-\exp[-2(x_{\mathrm{p}}-b)^{\frac{1}{2}}]), & x \geqslant b, \quad l = 1, \\ (1+s)(1-\exp[-2(x_{\mathrm{p}}-b)^{\frac{1}{2}}]), & x \geqslant b, \quad l = 2. \end{cases} \tag{4.2}$$

When $s = 0.25$, $b = 1$, figure 7(a) shows the evolution at $t = 16$, and at $t = 26$ (not shown) the trough in $l = 2$ continues to turn clockwise until it almost reaches the leading edge of $l = 2$, thereby tending to detach a negative eddy from the underlying boundary current. When s is increased to $s = 0.5$ (figure 7b) the result is similar except that the maximum on $l = 1$ is larger, and consequently the underlying positive vortices cause the leading edge of $l = 1$ to be displaced further away from $l = 2$. Notice that the common nosepoint is being over-run by the leading edge (minimum x) of the $l = 2$ interface. This effect would have been much more severe had we not automatically deleted a nosepoint when it was excessively over-run by the $l = 1$ interface. These deleted segments were so close to the boundary that negligible fluid areas and vorticies were involved.

These calculations delimit an endpoint ($\alpha = 1$) of the parametric regime, in which the boundary current propagates continually along the coast, and in all cases the speed of the leading edge of the intrusion was greater than 0.3. The figures also indicate the tendency for a negative nose eddy to form above the main boundary current.

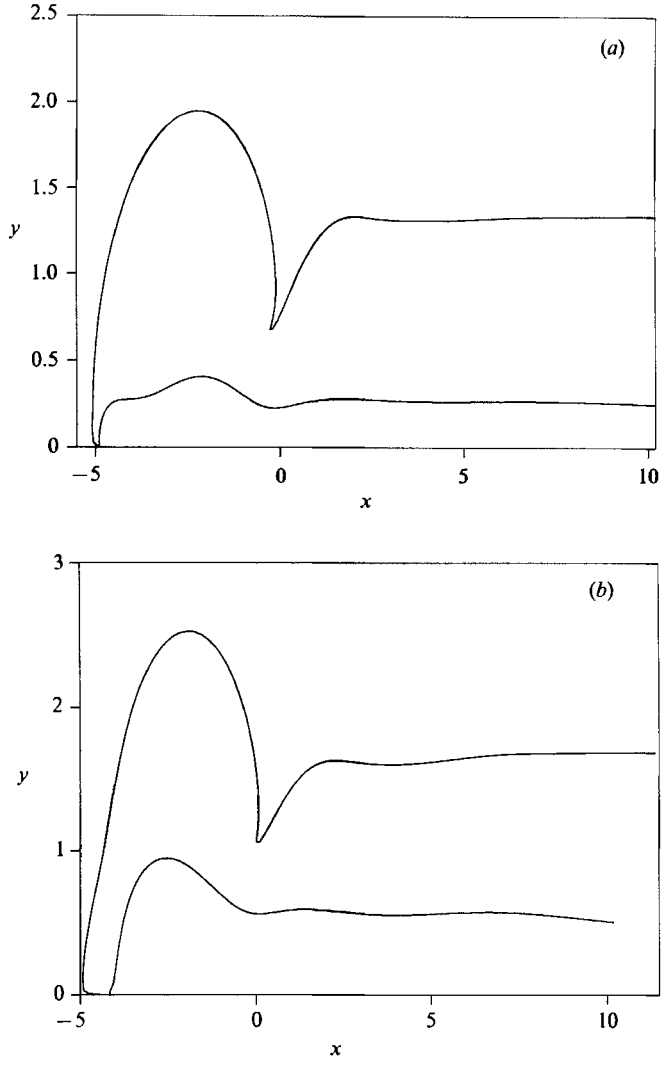

FIGURE 7. The evolution of the blunt nose (4.2), $t = 16$: (*a*) $s = 0.25$, (*b*) $s = 0.50$.

Next we consider $\alpha > 1$ in the $s = 0$ limit, corresponding to a half-jet having only negative vorticity between a single interface and the curved wall. Our previous qualitative remarks indicated that in this case separation from the boundary could not occur for any α, but it is important to do the computation for this case because the full algorithm (with $B(I, k) \neq 0$) is utilized for the first time. The number of segments used in the η-integration (equation (3.6)) increased from five to ten as the local value of the ordinate of the interface increased (preliminary runs doubling the number of segments gave insignificant changes). For the single interface the initial shape used (corresponding to (4.2)) was $y_p(x, 0) = 1 - \exp[-2(x-1)^{\frac{1}{2}}]$. When $\alpha = \frac{5}{4}$ (a 45° coastal deflection) the boundary current (figure 8*a*) and the nose eddy flow around the corner, and continue down the coast as expected. (Remember that the velocity is not zero in the irrotational fluid immediately outside the nose eddy.) A qualitatively similar result was obtained (figure 8*b*) when α was increased to $\alpha = \frac{3}{2}$, and at $t = 36$ there were 218 points on the interface.

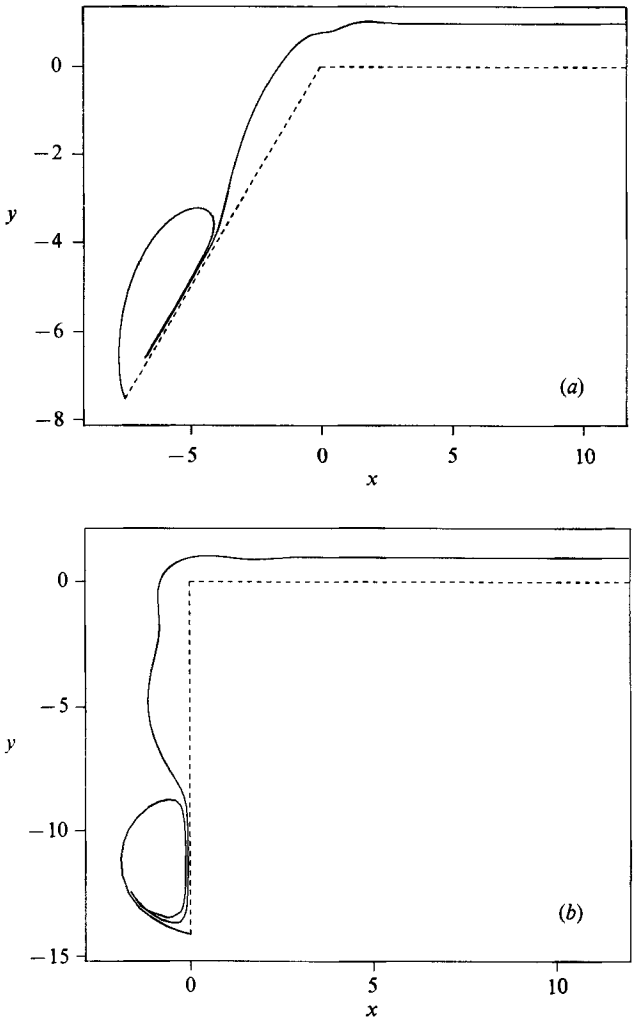

FIGURE 8. Flow of a half-jet ($s = 0$) around the corner of a wall: (*a*) $\alpha = \frac{5}{4}$, $t = 28$; (*b*) $\alpha = \frac{3}{2}$, $t = 36$.

The upper set of curves in figure 9 show the distance along the coast from the corner to the nose when $\alpha = \frac{3}{2}$ and when $\alpha = \frac{5}{4}$. The slope of the reference line labelled 'speed = $\frac{1}{2}$' corresponds to a nose velocity equal to the mean upstream velocity of the jet, and thus we see that the noses in figure 8 are almost moving with this mean speed. Similar speeds were obtained by Stern & Pratt (1985) for a straight coast.

The difference between the two curves ('area', 'c area') in the lower half of figure 9 gives an indication of the error in the numerical calculation. 'Area' is the integrated ordinate under the interface (in the truncated domain) minus the area of a reference rectangle of unit height extending from the corner ($x_p = 0$) to infinity. 'C area' is the corresponding area obtained from the mass conservation principle by integrating in time the known flux at $x_p = \infty$.

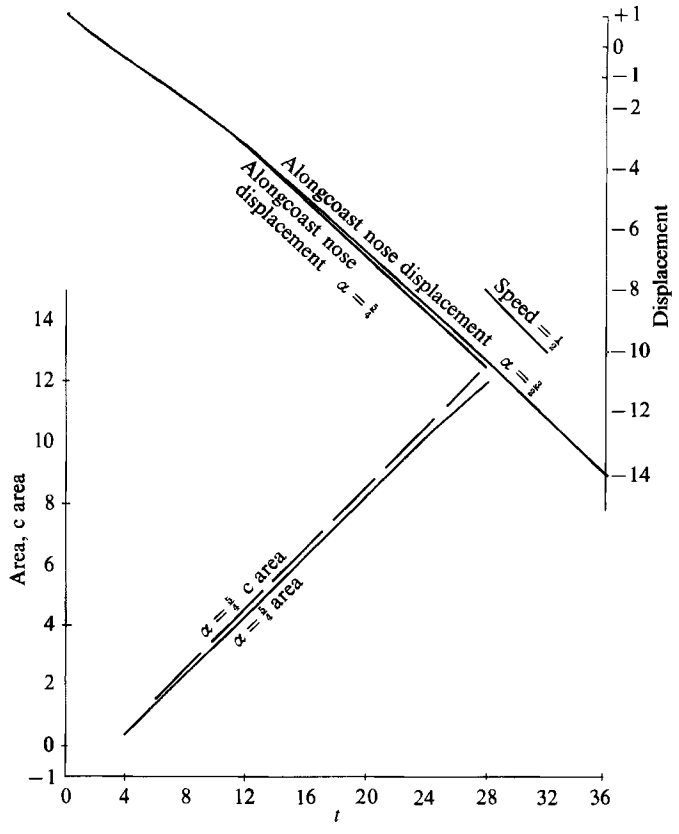

FIGURE 9. The two upper curves give the displacement of the nosepoint along the coast for the runs in figure 8. The final propagation speed is slightly less than $\frac{1}{2}$. The two lower curves give two independent calculations of the non-dimensional area bounded by the interface in figure 8(*a*). (See text.)

5. The full jet with $\alpha > 1$

The initial conditions for the following runs are given by (4.2) with $b = 1$. For a small $\theta \equiv \alpha - 1 = 18°$ and a small $s = 0.25$ (figure 10*a*) we obtain the expected non-separated flow at $t = 17$, in which the leading edge of the intrusion flows around the corner and continues along the downstream half of the coast. As previously mentioned, this progression of the leading edge reflects the dominant influence of the negative vorticity in the outer half of the jet. Except for the trough on $l = 2$ near $x = 0$, there were no noteworthy features in the full numerical domain ($x < 10.2$). The subscript p has been dropped here, and in all that follows.

By increasing the thickness of the positive layer to $s = 0.33$ (figure 10*b*) there is an increase in the downward and upstream velocities on the leading edge of $l = 1$, and this accounts for its large displacement from the leading edge of $l = 2$. Nevertheless, the current does not separate, and the velocity vectors (not shown) on $l = 1$ at $t = 11.1$ are all directed downstream and downcoast.

The effect of increasing the value of θ used in figure 10(*a*) is shown in figure 10(*c*). The leading edge ($l = 2$) of the intrusion at $t = 15.1$ still propagates downcoast with $u = -0.33$ at $x = -3.4$, but there is a marked difference in the behaviour of the leading edge of $l = 1$. The larger α produces a larger upstream velocity of positive-

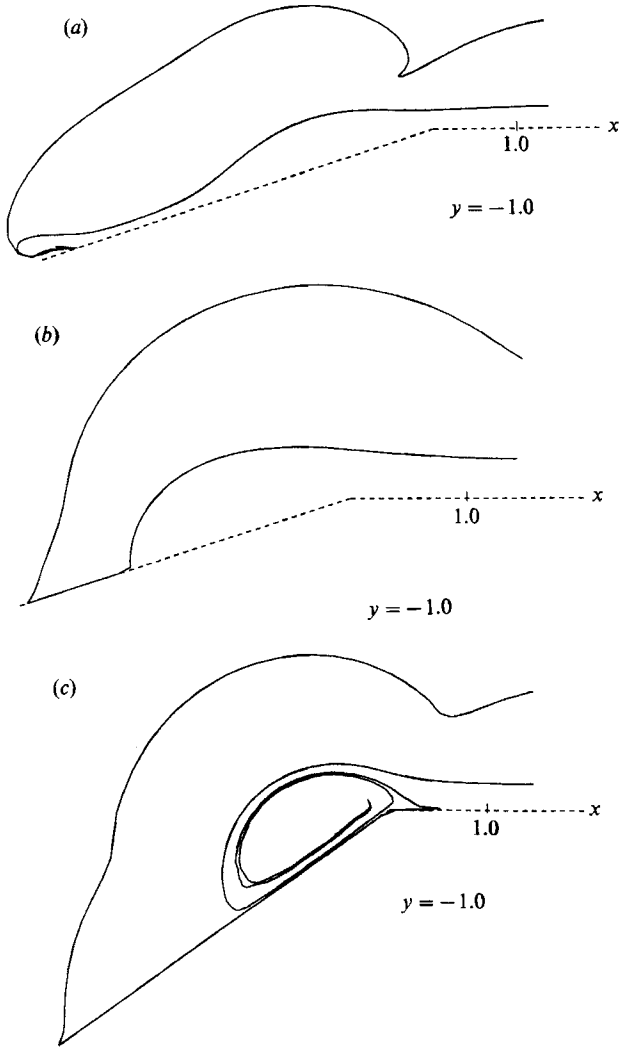

FIGURE 10. The flow of a full jet around the corner for the initial conditions (4.2). No vertical exaggeration. (*a*) $\alpha = 1.1$ (or $\theta = 18°$), $s = 0.25$, $t = 17$; (*b*) $\alpha = 1.1$, $s = 0.33$, $t = 11.1$; (*c*) $\theta = 36°$, $s = 0.25$, $t = 15.1$. The $l = 1$ interface starts at the common nosepoint ($x = -3.4$) and goes to ($x = 0.5$, $y = 0^+$) along a line which is indistinguishable from the wall. The interface then winds counterclockwise into the eddy, and then clockwise out. The interface continues clockwise to the endpoint $x = 10.2$.

vorticity particles near the corner, the result of which causes the leading edge of the $l = 1$ interface to stagnate, and thus the fluid (under $l = 1$) further upstream flows into a large positive 'wake' eddy. The common nosepoint is at $x = -3.4$, and the $l = 1$ interface is almost coincident with the wall from this point to $x \approx 0.5$, after which it winds into, and then out of the positive eddy. This winding effect started at $t = 8.1$, when the leading edge of $l = 1$ had a simple shape similar to the one in figure 10(*b*). At later times (figure 10*c*) we see that the positive eddy entrains a small amount of negative-vorticity fluid in the winding.

Increasing s to 0.33 (figure 11*a*) increases this entrainment. At $t = 16.2$ the nominal nosepoint has actually retrogressed upstream to the corner! To all intents

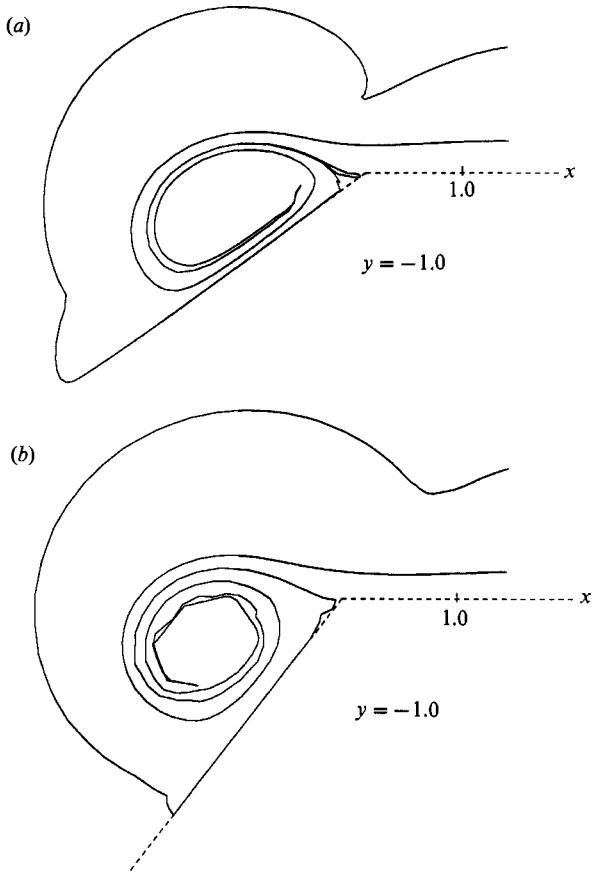

FIGURE 11. (*a*) $\theta = 36°$, $s = 0.333$, $t = 16.2$. The $l = 2$ interface begins at the common nosepoint ($x = 0^-$), follows the $l = 1$ interface for a short interval, and then comes back towards the wall. It then proceeds to the minimum x along a line which is indistinguishable from the wall, and then $l = 2$ turns clockwise. The $l = 1$ interface starts at the corner and winds into the eddy. (*b*) $\theta = 52.2°$, $s = 0.25$, $t = 14.1$.

and purposes, however, we may say that further downstream there is a different nosepoint for $l = 2$, for example at $x = -2.8$ where the distance of the interface from the wall is only 10^{-2}, and the x-component of velocity is $u = -0.37$. Note the very small wedge of irrotational fluid at the corner which is also being entrained into the eddy. Although one may say that a positive-vorticity eddy has detached from the wall, the entire current has not separated, because a portion of it has continued to flow along the downstream part of the wall. Thus if all of the rotational fluid in the jet at $t = 0$ had been coloured (as in our laboratory experiment), then some of this coloured fluid would appear along the downstream half of the wall at $t = 16.2$ (figure 11*a*).

When the value of θ used in figure 10(*c*) is increased further the positive eddy is displaced further from the wall, as indicated in figure 11(*b*) for $\theta = 52.2°$, $s = 0.25$. At $t = 15.1$ (not shown) the common nosepoint is at $x = -1.89$ where $u = -0.20$. We also note that considerably more negative vorticity is being entrained in this case than in any of the previous ones.

Before proceeding to examples of 'separation' it is necessary to have an

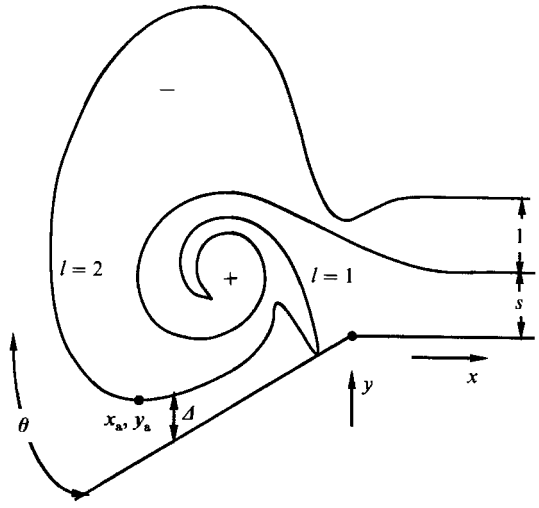

FIGURE 12. Definition diagram for separation. See text.

operational definition of it, especially because our calculations are of limited temporal extent. The sketch (figure 12) of a separated flow shows irrotational fluid between the wall and the eddy, so that none of the previously mentioned coloured fluid flows along the wall downstream from the corner. At the minimum point on $l = 1$ the coordinates are (x_a, y_a), the horizontal velocity is u_a, and the minimum separation of the vortical fluid from the coast is denoted by Δ. We say that the jet separates if (at the last time of our integration) $u_a > 0$, and $\Delta > 0$ is increasing with time. No separation occurs if $u_a < 0$ and $|x_a|\tan\theta - |y_a|$ is very small compared to $|y_a|$, i.e. Δ is virtually zero.

A clear example of a separated jet, in which all the previously stated conditions are satisfied, occurs for $s = 0.5$, $\alpha = 1.29$ (figure 13a). It seems likely that for $t \gg 15.1$ the trough on $l = 2$ (near $x = 0.5$) will continue to amplify and approach the $l = 1$ interface, whereupon irrotational fluid will wind into a negative-vorticity eddy at the leading edge of the jet, thereby forming a dipolar structure (see figure 16b below). The elementary calculation in the Appendix (figure 3) suggests that the dipole will continue to increase its distance from the wall as time increases. (A numerical calculation of this would have to employ contour 'surgery' on the windings in the eddy, with due regard for the entrainment effects.)

A similar result is obtained (figure 13b) when the coastal angle is reduced to 45°. Figure 13(c) shows the separation for a smaller s and a larger θ. We then keep $s = 0.33$ constant and reduce θ successively (figure 14a, b), thereby approaching the transitional regime.

Figure 15 shows that for a large $s = 1.0$ only a small θ is required for separation, and there is a relatively large flow reversal which penetrates upstream from the corner. This suggests that under certain circumstances the point of separation at a smooth coast may be located at a considerable distance upstream from the maximum wall curvature.

The effect of changing the initial condition from a 'blunt' nose intrusion to a 'sharp' nose intrusion (i.e. equation (4.1) with $b = 1$) is indicated in figure 16(a) for the case $s = 0.5$, $\alpha = 1.25$. At the earlier time $t = 10$ the nosepoint had advanced to $x = -1.26$ with $u_a = -0.10$, but a rapid retrogression of the nosepoint began at $t \approx$

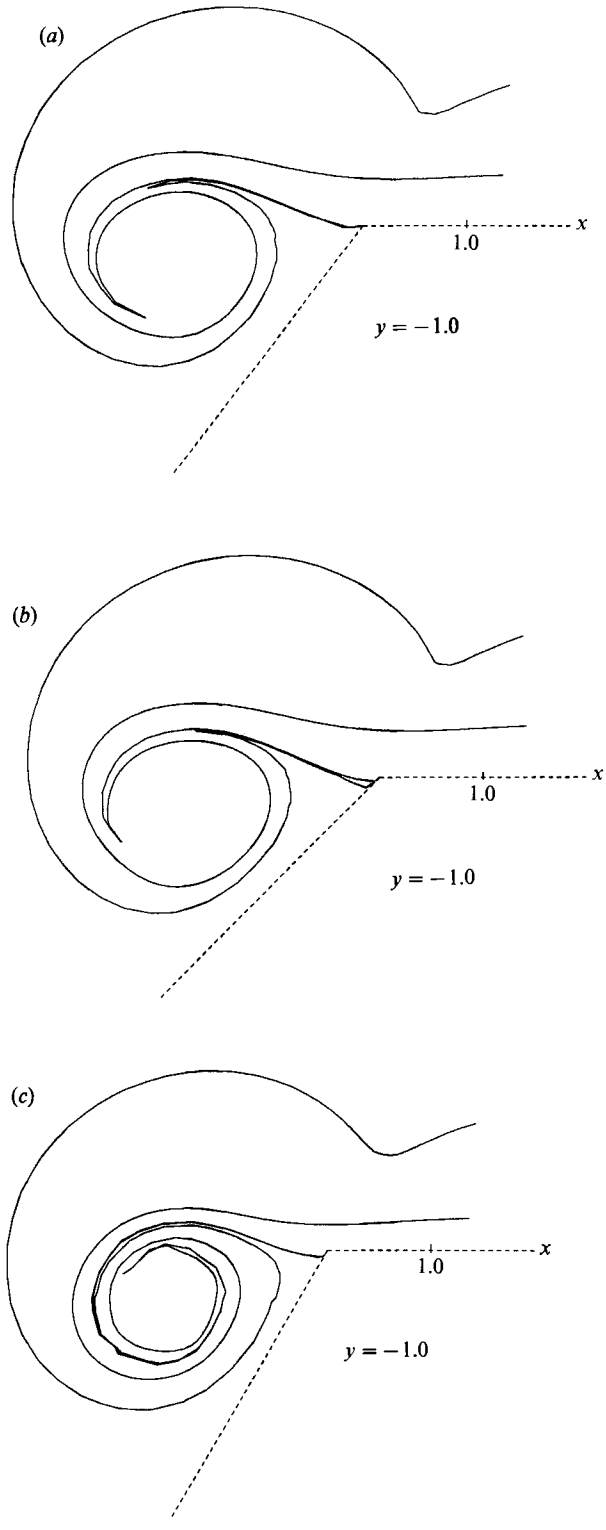

FIGURE 13. Example of separation: (*a*) $\theta = 52.2°$, $s = 0.5$, $t = 15.1$. The nosepoint is near $x = 0$. (*b*) $\theta = 45°$, $s = 0.5$, $t = 15.1$. (*c*) $\theta = 60°$, $s = 0.333$, $t = 15.2$.

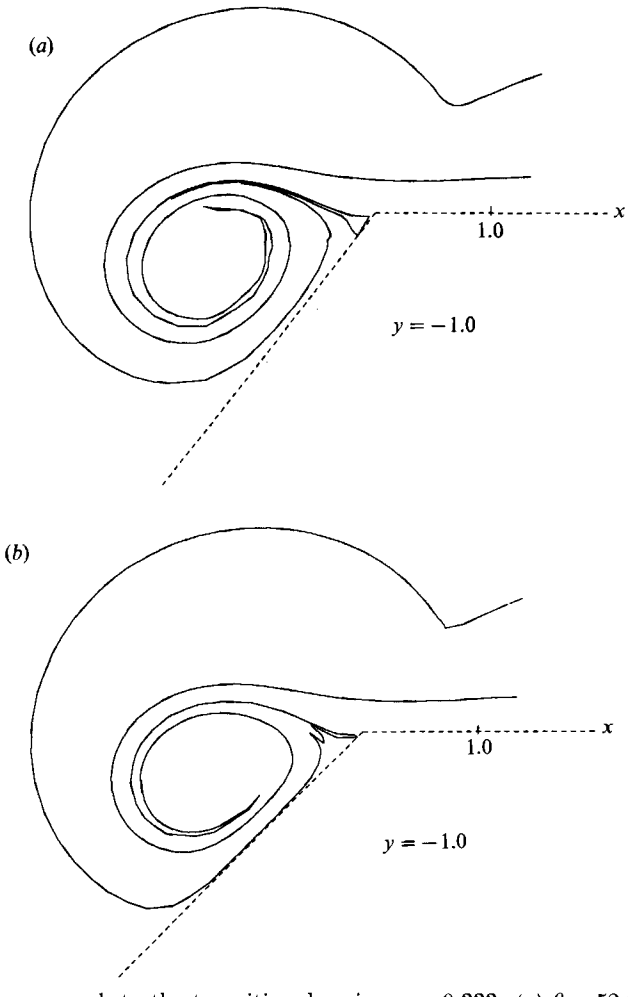

FIGURE 14. The approach to the transitional regime $s = 0.333$: (*a*) $\theta = 52.2°$, $t = 14.7$. (*b*) $\theta = 45°$, $t = 14.2$.

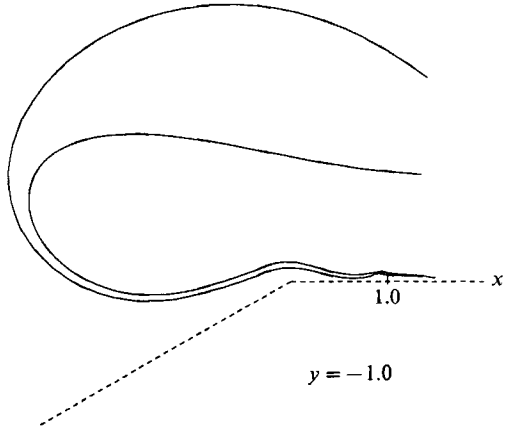

FIGURE 15. $\theta = 30°$, $s = 1.0$, $t = 12.1$. Note that separation here occurs upstream of the 'curved' part of the boundary.

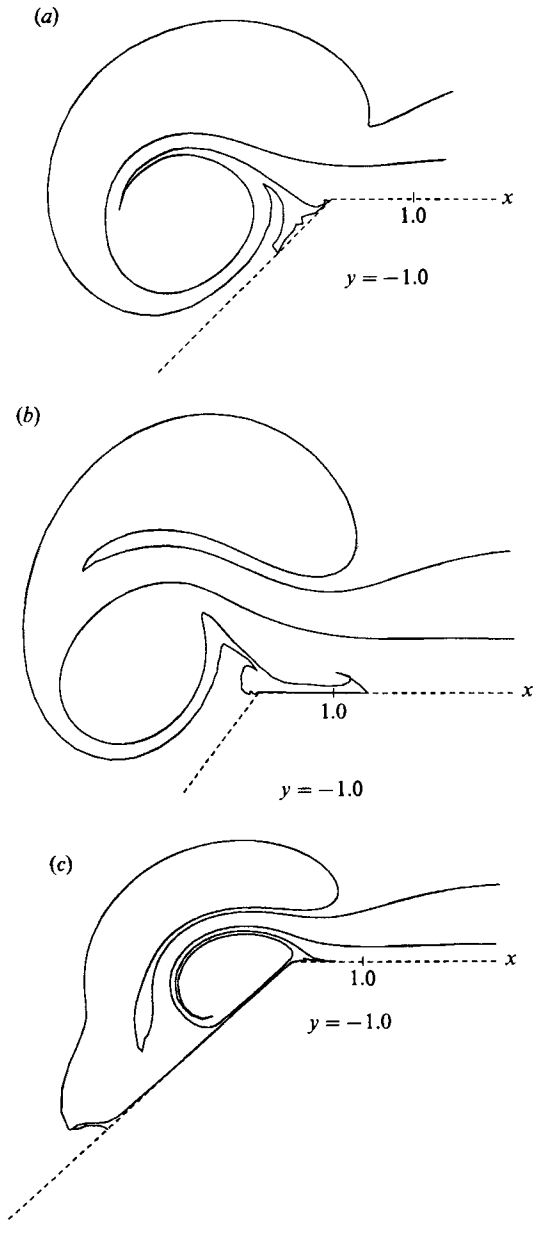

FIGURE 16. These runs show that a change in shape of the initial interfaces does not greatly alter the separation criterion: (*a*) using (4.1) with $\theta = 45°$, $s = 0.5$, $t = 16$; (*b*) using the bulbous nose (4.2)–(4.3) with $s = 0.5$, $\alpha = 1.25$, $t = 11$; (*c*) the bulbous nose with $s = 0.25$, $\alpha = 1.25$, $t = 13$.

14. At $t = 16$ the nosepoint velocity is $u = +0.16$, $u_a > 0$, and thus we see that the conditions for separation are satisfied. In fact, the result is quite similar to the blunt-nose result in figure 13(*b*), which has the same s, α. As in figure 9 we computed the rate of increase in area beneath $l = 2$ in two different ways (one from the numerical results and the other from the conservation of mass) and found a discrepancy of 10%, most of which could be explained by the small finite vertical velocity in the vicinity of the $x = 10.2$ endpoint.

A few calculations were also made to examine the effects of changing the initial

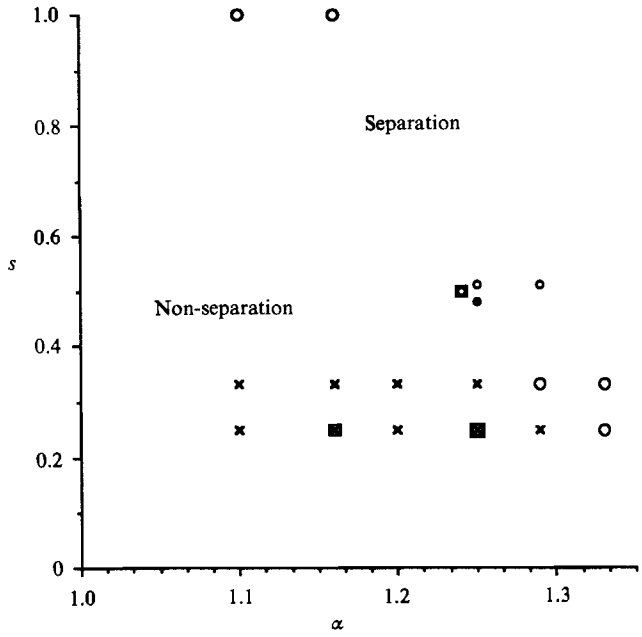

FIGURE 17. Regime diagram. Circled points indicate numerical runs in which the jet separated from the boundary. Points × indicate non-separated flows. Points surrounded by a square are for (4.3). The solid circle is for (4.1).

condition from the 'blunt' nose one in (4.2) to a more 'bulbous' one. Accordingly (4.2) was multiplied by

$$1+\frac{1}{1+(x-2)^2} \tag{4.3}$$

so that $y_p(x,0)$ reaches its maximum value at $x \approx 2$, and then decreases slowly until the asymptotic ordinate (s or $(1+s)$) is reached. The bulbous-nose calculation for $s = 0.5$, $\alpha = 1.25$, $t = 11$ (figure 16*b*) shows a pronounced dipole at the leading edge of the separated jet. The thin filament of irrotational fluid intruding into the negative-vorticity region is the result of the evolution of the $l = 2$ trough (cf. figure 13*c*). When s is reduced to $s = 0.25$, with $\alpha = 1.25$ held at the same value, we see (figure 16*c*) that no separation occurs, and the bulbous $l = 2$ nose of the jet proceeds downstream ahead of the wake eddy ($l = 1$). The common nosepoint on the wall is at $x \approx 2.5$. A similar result was obtained for $s = 0.25$, $\alpha = 1.666$ (not shown).

The regime diagram for all runs is given in figure 17: × symbols indicate jets which do not separate, and circles indicate separation. The 'sharp' nose initial condition corresponds to the solid circle, and the bulbous nose initial condition corresponds to points surrounded by a square. Not shown on this diagram are all the $\alpha = 0$ runs in which separation did not occur, and all the $s = 0$ runs in which separation also did not occur. The reader can easily visualize a curve running from the lower right corner to the upper left corner of the diagram, which delimits the separating/non-separating flows.

For later reference we note (figure 17) that the critical α, which delimits the separating from the non-separating flows, is $\alpha = 1.27 \pm 0.02$ at $s = 0.33$.

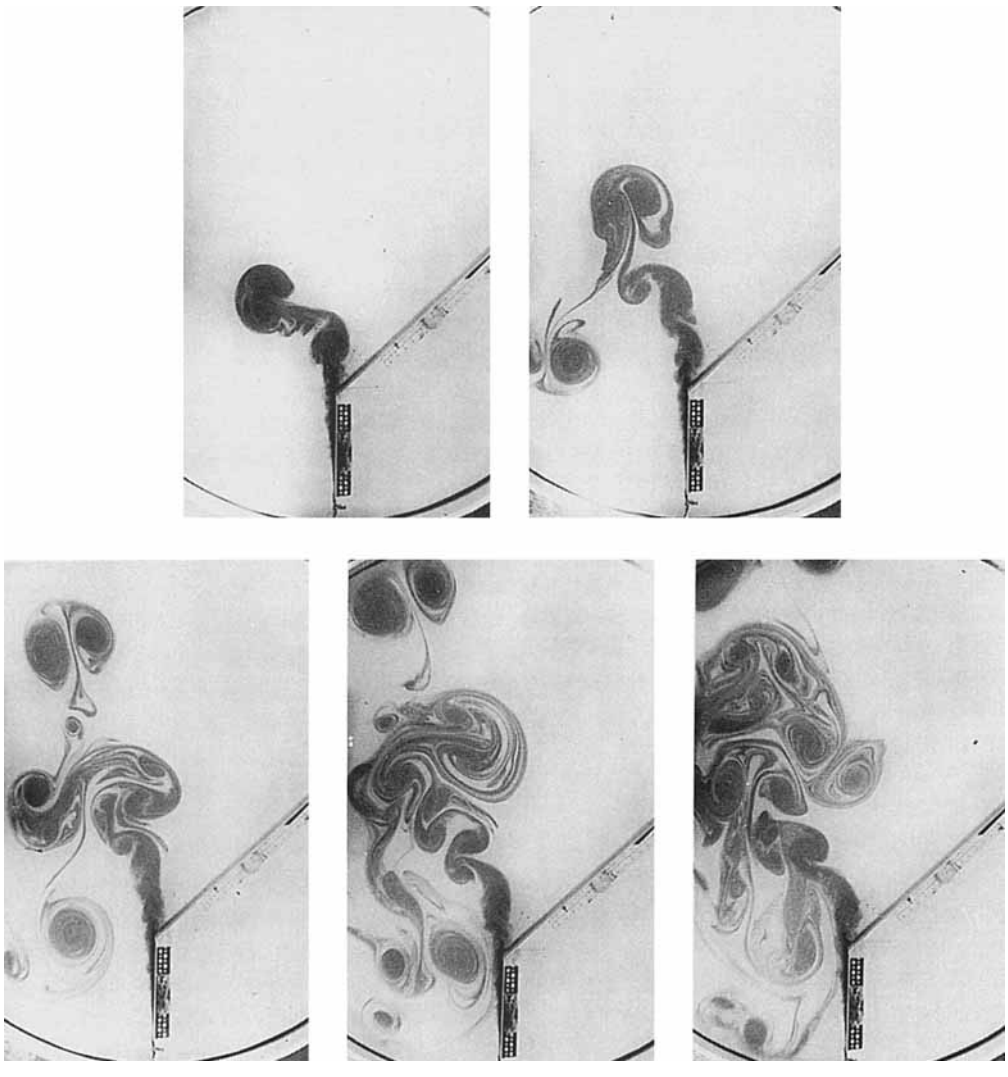

FIGURE 18. Top view of a dyed jet which flows from a source (at the bottom) and separates from the wall at the corner point. The parameters for this run are $\theta = 50°$ and $QT^{\frac{1}{2}} = 28.5$ c.g.s., where T is the rotation period of the tank. Photographs are 1 min. apart, starting at top left and ending at bottom right. The distance of the nozzle from the corner (35 cm) and Q are half the values used in figure 1.

6. Experiment

In these preliminary experiments the simplest technique was used to produce a wall jet. Accordingly three horizontal nozzles (4.76 cm long and 0.14 cm diameter) were mounted flush against the sheet metal wall at depths of 6, 10, and 14 cm in water 20 cm deep. The nozzles were soldered to a manifold connected to a flowmeter and a pump in a reservoir. Because of the complexity of the evolving flow from the source, we decided to keep the nozzles at a fixed distance (35.2 cm) from the corner in all the quantitative runs discussed in this section and plotted in figure 21. (This distance is half that used in the illustrative run in figures 1 and 2.) Despite the three-dimensionality of the flow emerging from the nozzles, a depth-independent flow was

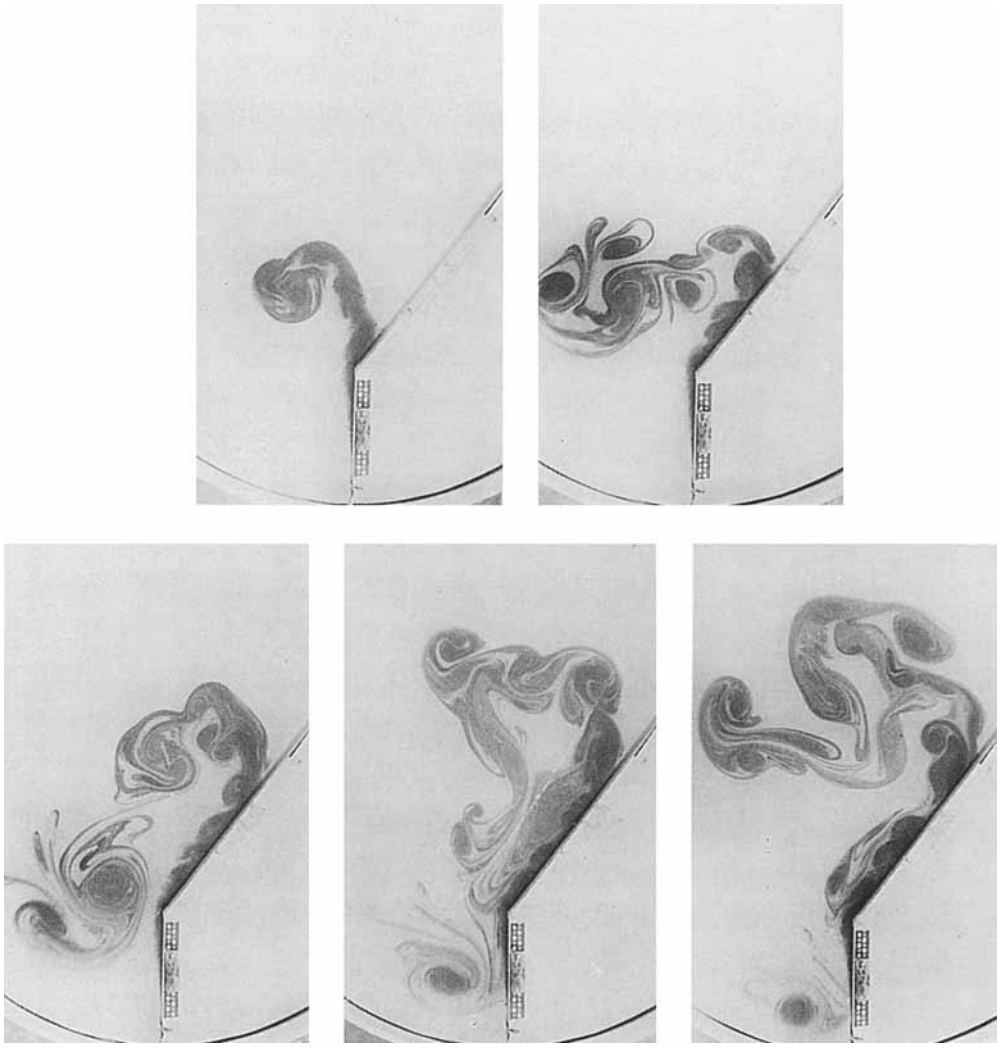

FIGURE 19. Top view of a dyed jet which flows from a source around the corner without separating at that point (see text). The parameters for this run are $\theta = 30°$ and $QT^{\frac{1}{2}} = 28.5$. Photographs are 1 min. apart. The white dots in the photographs are floating pellets of cardboard.

realized 15 cm downstream from the nozzle. This was indicated by unmistakable vertical dye columns ('Taylor Inkwalls'), and confirmed by the velocity measurements to be discussed. At the corner of the wall there was a flexible joint which allowed the downstream part to be set at any (clockwise) angle θ relative to the upstream part.

In the separating flow shown in figure 18 the value of Q (as well as the distance of the nozzle from the corner) is half the value used in figure 1, and θ is 10° smaller (but the rotation period T is the same). The state of the coastal current before the nose reaches the corner is qualitatively similar to the early times in figure 1.

The early phases of the non-separating flow shown in figure 19 are similar to those in figure 2, the main difference being that the large anticlockwise eddy which forms when the nose encounters the corner behaves somewhat differently with respect to

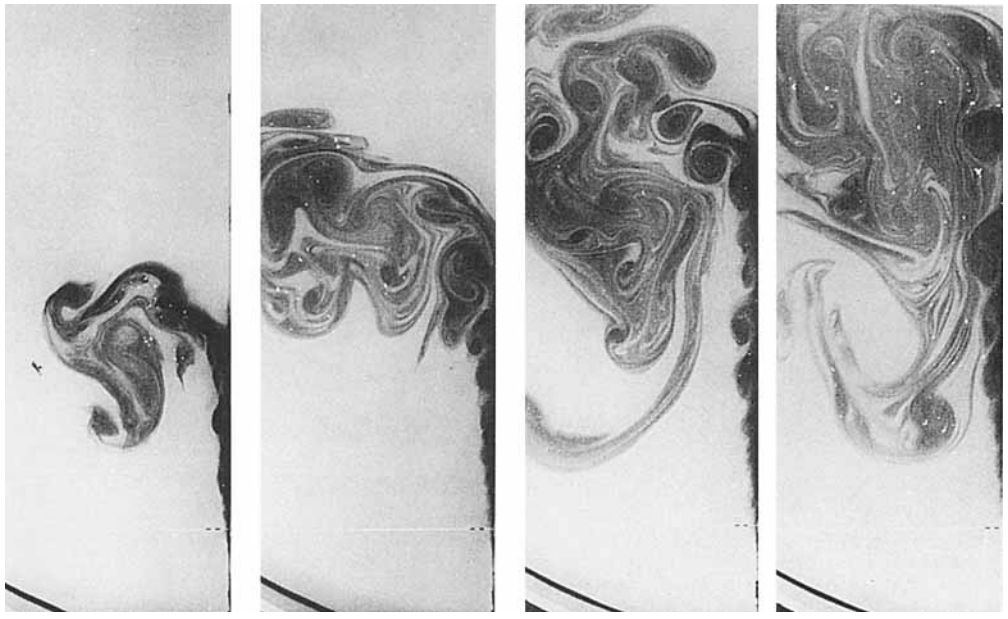

FIGURE 20. Four experiments with a jet along a straight wall. Each photograph is taken 5 min. after the start of the run. Starting at the top the flow rates in cc s^{-1} are 2.6, 4.2, 5.7 and 6.7. In each case the wall jet stagnates, and the oncoming fluid is ejected into the interior. But this kind of 'separation' occurs 'far' downstream (where cumulative entrainment and friction become important), and it should be distinguished from the separation occurring in figure 19.

the jet flowing past the corner. As the jet continues along the downstream half of the wall, instabilities develop, irrotational fluid is entrained, the nose slows down, and fluid is then ejected normal to the wall. The same effects occur for a straight wall, as shown by the four different runs in figure 20. (See the similar effect in the density current in Stern, Whitehead & Hua 1982.) Although this kind of separation (over large x, t intervals) is interesting and worthy of further study, it must be clearly differentiated from that which occurs at the corner. According to our criterion 'separation' occurs if no dye flows along the wall downstream from the corner.

The difference between a separating and a non-separating flow was always clear cut, reproducible, and easy to map in the regime diagram (figure 21). Aside from θ only the source flow and rotation period were varied in these runs, and a critical $\theta_c = 45° \pm 5°$ is suggested for $QT^{\frac{1}{2}}$ larger than ~ 20 c.g.s. The ordinate in figure 21 is proportional to the Rossby number of the jet divided by the square root of the Ekman number, this being the ratio of inertial to bottom friction terms in the vorticity equation. In order to non-dimensionalize the ordinate we need the jet width, but the estimates of this given later are not adequate for exploring the full parametric regime, so that we cannot say that the Rossby and Ekman numbers form the complete non-dimensional group. There is also a lateral Reynolds number $Q/(\text{depth} \times \text{viscosity})$. Although this is not as large as we would like, there is no systematic dependence on it (table 1). Some variability of θ_c in figure 21 is suggested at the smallest values of $QT^{\frac{1}{2}}$, but this is certainly not definitive.

Velocity measurements in the jet were obtained in separate runs using a straight wall. Neutrally buoyant pellets (~ 0.5 mm) were injected near the nozzle, and streak photographs were taken one minute after startup at a distance 20–30 cm downstream

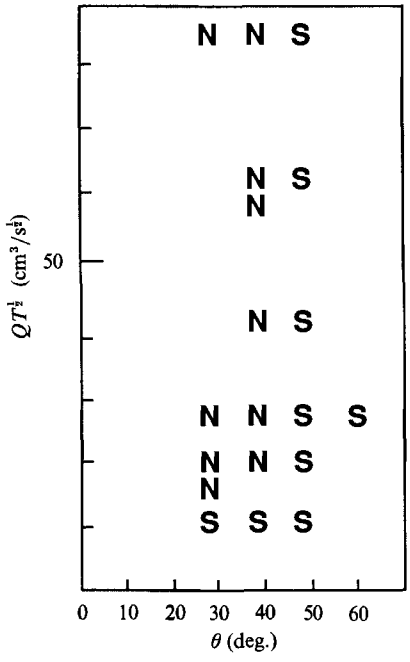

FIGURE 21. Regime diagram showing separation (S) or non-separation (N) of the jet as a function of $\theta, Q. T$ for a fixed nozzle position.

Run number	T (s)	Q (cc/s)	θ (deg.)	$QT^{\frac{1}{2}}$	Result
6294	15.1	7.32	60	28.4	Separation
761	15.1	7.32	0	28.4	Non-separation
762	15.1	7.32	30	28.4	Non-separation
763	15.1	7.32	40	28.4	Non-separation
764	15.1	7.32	50	28.4	Separation
771	15.15	2.58	50	10.0	Separation
772	15.15	16.25	50	63.2	Separation
773	15.15	2.58	40	10.0	Separation
774	15.15	16.25	40	63.2	Non-separation
775	15.15	2.58	30	10.0	Separation
791	62.7	2.58	30	20.4	Non-separation
792	inf.	2.58	30	inf.	Different regime
7101	64.01	2.58	30	20.8	Non-separation
7102	15.07	16.25	30	62.9	Non-separation
7103	29.5	16.25	30	88.3	Non-separation
7104	29.5	16.25	40	88.3	Non-separation
7105	29.5	16.25	50	88.3	Separation
7106	15.76	5.67	50	22.5	Separation
7108	15.76	10.8	50	42.9	Separation
7109	15.37	5.67	40	22.2	Non-separation
71010	15.37	10.8	40	42.3	Non-separation

TABLE 1. Summary of experiments with a corner

(this position is slightly upstream of the corner in the separation runs). Pellets in the 5–15 cm depth range were illuminated from the side and photographed from above using a 1 s exposure every 2 s. The maximum velocity was 5 cm/s, and the main errors due to parallax, pellet size, and digitizing were estimated to total less than 10 %. From these observations we were also able to ascertain the depth independence of the velocities.

The measurements for four values of $QT^{\frac{1}{2}}$ are shown by the open squares in figure 22(*a–d*). The large amount of scatter is due to x,t-variations caused by the two-dimensional waves and eddies in the jet. (But regions of the flow containing very large and visually obvious eddies at the outer edge of the jet were (subjectively) excluded from the sample.) The solid points drawn in these figures were obtained using running mean values of the individual measurements. From these curves a crude estimate of a theoretical s was made by visually fitting a triangular profile to the mean curve, with a bias towards capturing the extreme values of vorticity in the outer and inner regions of the jet. (It is believed that these values, rather than the associated geometrical connotation of s in the theoretical model, are the significant physical parameters.) In this way we arrived at a mean $s \approx 0.3$ with perhaps a factor of two uncertainty. This s-value and the experimental $\theta_c = 45° \pm 5°$ are consistent with the theoretical value $\theta_c = 1.27 \pm 0.02$ rad. $= 49°$, for $s = 0.33$, but the extent of the quantitative agreement must be regarded as fortuitous.

7. Conclusion

An inviscid piecewise-uniform vorticity model has been used to examine the flow of a barotropic jet around a sharply curved wall. For a given ratio s of the magnitude of the 'offshore' vorticity to the 'inshore' vorticity, the jet will separate at the corner if θ exceeds a critical angle (figure 17). The onset of this process (figure 13) is characterized by the formation of a dipole vortex at the leading edge of the jet, when it reaches the corner. The upstream jet then flows into this dipole, which also entrains ambient irrotational water. Although our contour-dynamical calculations are limited in time, it is strongly suggested that the dipole propagates into the interior basin, and thereby establishes a permanently separating jet at the corner. For non-separating conditions, on the other hand, the main part of the upstream jet turns the corner and continues flowing along the coast (figure 10). The transition from the non-separated to the separated regime is illustrated by figure 11(*a*, *b*), in which a cyclonic wake vortex forms in the lee of the curved coast. The vortex may eventually be carried downstream by the current in which it is embedded, and then the process may repeat.

Although the Coriolis parameter does not enter explicitly into this theory, the basic rotation in the laboratory experiment has the crucial effect of suppressing three-dimensional turbulence, and giving rise to a two-dimensional flow. In our exploratory experiments the source geometry was kept constant, the flow rate Q was varied, as were the rotation rate and the corner angle θ. Except for relatively small Q we found that the critical θ for separation was $45° \pm 5°$. From velocity measurements we estimated the value of s, computed θ_c from the piecewise-uniform vorticity model, and found consistency with the observed θ_c. The theory (figure 17) indicates that the critical θ should decrease as s increases, and this might partially explain the decrease of θ_c in figure 21 as Q decreases. The observed qualitative nature of the onset of separation (figure 1) is also consistent with the bulbous-nose calculations in figure 16(*b*). The qualitative discussion of the inviscid separation

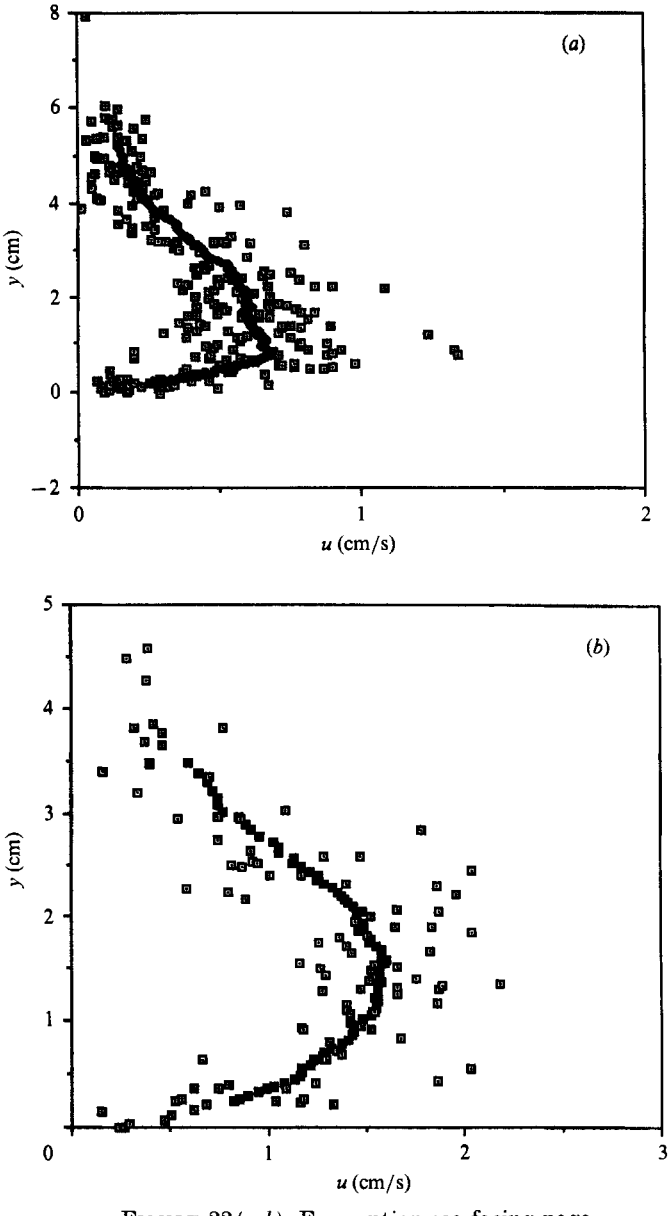

FIGURE 22(a, b). For caption see facing page.

mechanism in figure 4 indicates that similar effect should occur when a high-Reynolds-number jet flows along a smoothly curving boundary.

We thank Mr S. Turner of FSU for programming assistance, and Mr B. Frazel of WHOI for experimental assistance. Partial financial support of the theoretical work from ONR is acknowledged, and the laboratory experiments were supported by NSF grant OCE86-14842.

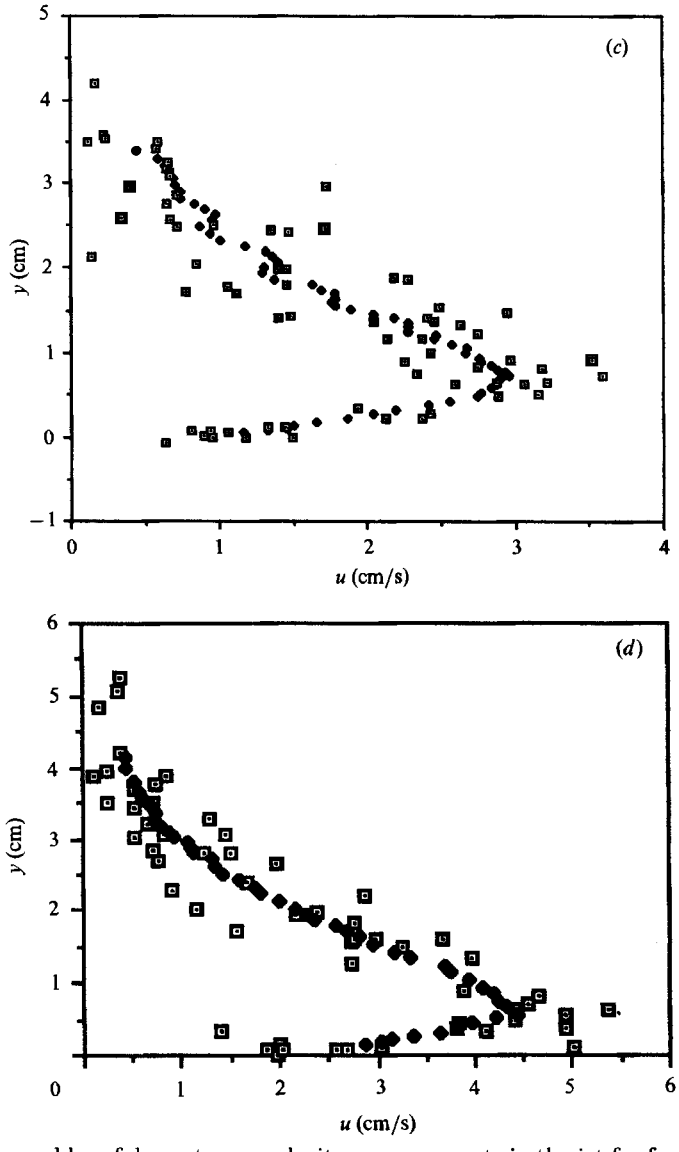

FIGURE 22. Ensembles of downstream velocity measurements in the jet for four different runs (see text) (*a*) $QT^{\frac{1}{2}} = 10.0$, the solid curve is a 41 point running mean; (*b*) $QT^{\frac{1}{2}} = 15.5$ solid points give a 21 point running mean; (*c*) $QT^{\frac{1}{2}} = 22$, solid points give an 11 point running mean; (*d*) $QT^{\frac{1}{2}} = 28.8$ solid points give an 11 point running mean.

Appendix. Separation of dipolar point vortices

We compute here the conditions necessary for a dipolar point vortex (figure 3) to separate from a bent wall by moving to infinite distances from it. This elementary problem not only provides insight into the numerical calculations of §5, but supplements these by suggesting the evolution of the latter over a longer timespan.

We recall (cf. (3.1*a*)) that the complex function

$$F(\zeta) = \frac{\mathrm{i}}{2\pi}\ln\left(\frac{\zeta^\beta - z_+^\beta}{\zeta^\beta - \bar{z}_+^\beta}\right) - \frac{\mathrm{i}}{2\pi}\ln\left(\frac{\zeta^\beta - z_-^\beta}{\zeta^\beta - \bar{z}_-^\beta}\right)$$

is analytic for $2\pi > \arg\zeta \geqslant 0$ except at the locations of the positive vortex $\zeta = z_+(t)$ and the negative vortex $\zeta = z_-(t)$. If ζ_b denotes a point on either half of the bent wall then $\zeta_b^\beta = \zeta_b^{1/\alpha}$ is either a real positive number or a real negative number $[(e^{i\pi\alpha})^{1/\alpha} = -1]$, so that ζ_b^β equals its complex-conjugate (denoted by a bar). Therefore the imaginary part of $F(\zeta)$ is a stream function, vanishing on the bent wall, vanishing at $|\zeta_b| = \infty$, and satisfying Laplace's equation (except at z_+, z_-). Moreover $\overline{dF/d\zeta}$ has an imaginary part equal to the x-component of the stream function, and a negative part equal to the y-derivative of the stream function. Therefore $-dF/d\zeta$ is the complex velocity vector associated with the stream function. Finally we note that the limit of the first logarithmic term in $F(\zeta)$ as $\zeta \to z_+$ is $\ln|\zeta - z_+| + \ldots$, so that the circulation about z_+ is $+1$, and the circulation about z_- is -1. Thus $-\overline{dF/d\zeta}$ gives the velocity vectors produced by the point vortices having unit circulation.

In order to compute the velocity with which the vortex at z_+ moves we must average $-\overline{dF/d\zeta}$ in a small circle surrounding z_+, which is equivalent to discarding the term containing the pole $[(z-z_+)^{-1}]$ in the Laurent expansion. Thus we get

$$\frac{2\pi}{i}\lim\frac{dF}{d\zeta} = \left[\lim\frac{\beta\zeta^{\beta-1}}{\zeta^\beta - z_+^\beta}\right] - \frac{\beta z_+^{\beta-1}}{z_+^\beta - \overline{z_+^\beta}} - \frac{\beta z_+^{\beta-1}}{z_+^\beta - z_-^\beta} + \frac{\beta z_+^{\beta-1}}{z_+^\beta - \overline{z_-^\beta}},$$

and the bracketed term becomes

$$\frac{\beta z_+^{\beta-1} + \beta(\beta-1)\, z_+^{\beta-2}(\zeta - z_+) + \ldots}{\beta z_+^{\beta-1}(\zeta - z_+) + \frac{1}{2}\beta(\beta-1)\, z_+^{\beta-2}(\zeta - z_+)^2 + \ldots} = \frac{1}{\zeta - z_+}\,\frac{1 + (\beta-1)\, z_+^{-1}(\zeta - z_+) + \ldots}{1 + \dfrac{\beta-1}{2} z_+^{-1}(\zeta - z_+)}$$

$$= \left(\frac{1}{\zeta - z_+}\right) + \frac{\beta-1}{2z_+} + \ldots.$$

We now discard the term in parenthesis since it has zero average around a circle surrounding z_+, and thus we get

$$\frac{2\pi}{i\beta}\frac{dz_+}{dt} = -\frac{\overline{z_+^{\beta-1}}}{\overline{z_+^\beta} - z_+^\beta} - \frac{\overline{z^{\beta-1}} +}{\overline{z_+^\beta} - \overline{z_-^\beta}} + \frac{\overline{z_+^{\beta-1}}}{\overline{z_+^\beta} - z_-^\beta} + \frac{\beta-1}{2\overline{z_+}\beta}.$$

Likewise, for the motion of the anticyclonic point vortex we get

$$\frac{2\pi}{i\beta}\frac{dz_-}{dt} = \frac{\overline{z_-^{\beta-1}}}{\overline{z_-^\beta} - z_+^\beta} - \frac{\overline{z_-^{\beta-1}}}{\overline{z_-^\beta} - z_+^\beta} + \frac{\overline{z_-^{\beta-1}}}{\overline{z_-^\beta} - z_-^\beta} - \frac{\beta-1}{2\overline{z_-}\beta}.$$

By using $$z_+ = C^\alpha, \quad z_- = A^\alpha, \quad \frac{\beta^2}{2\pi}t = \tau,$$

The above equations simplify to

$$\frac{dC}{d\tau} = \frac{i}{(C\bar{C})^{\alpha-1}}\left[-\frac{1}{\bar{C}-C} - \frac{1}{\bar{C}-\bar{A}} + \frac{1}{\bar{C}-A} + \frac{1-\alpha}{2\bar{C}}\right],$$

$$\frac{dA}{d\tau} = \frac{i}{(A\bar{A})^{\alpha-1}}\left[\frac{1}{\bar{A}-\bar{C}} - \frac{1}{\bar{A}-C} + \frac{1}{\bar{A}-A} - \frac{1-\alpha}{2\bar{A}}\right].$$

For the initial conditions stated in the caption of figure 3 we have

$$C(0) = e^{\pi i/2\alpha}, \quad A(0) = (1+\sigma)^{1/\alpha}C(0).$$

For $\alpha = 1.25$ the temporal integration showed both vortices remaining together and moving away from the boundary (separating) when $\sigma(0) < 2.85$. This critical distance increased to 3.75 for $\alpha = 1.5$.

REFERENCES

ACTON, E. 1976 Large eddies in a two-dimensional shear layer. *J. Fluid Mech.* **76**, 561.

DENNIS, S. C. R. & CHANG, G. Z. 1970 Numerical solutions for flow past a circular cylinder. *J. Fluid Mech.* **52**, 471.

FLIERL, G. R., STERN, M. E. & WHITEHEAD, J. A. 1983 The physical significance of modons: laboratory experiments and general integral constraints. *Dyn. Atmos. Oceans* **7**, 233.

OU, H. W. & DE RITTER, W. P. M. 1986 Separation of an inertial boundary current from an irregular coastline, *J. Phys. Oceanogr.* **16**, 280.

PARSONS, A. T. 1969 A two layer model of Gulf Stream separation. *J. Fluid Mech.* **39**, 511.

ROED, L. P. 1980 Curvature effects on hydraulically driven inertial boundary currents. *J. Fluid Mech.* **96**, 395.

SHEFFIELD, J. S. 1977 Trajectories of an ideal vortex pair near an orifice. *Phys. Fluids*, **20**, 543.

SHEN, C. Y. 1981 The rotating hydraulics of the open-channel flow between two basins. *J. Fluid Mech.* **112**, 161.

SMITH, F. T. 1986 Steady and unsteady boundary layer separation. *Ann. Rev. Fluid Mech.* **18**, 197.

STERN, M. E. 1989 Evolution of a locally unstable shear flow near a wall or a coast. *J. Fluid Mech.* **198**, 79.

STERN, M. E. & PRATT, L. 1985 Dynamics of vorticity fronts. *J. Fluid Mech.* **161**, 513.

STERN, M. E., WHITEHEAD, J. A. & HUA, B. L. 1982 Intrusion of a density current along a coast. *J. Fluid Mech.* **123**, 237.